



# Precipitation and Release of Solar Energetic Particles from the Solar Coronal Magnetic Field

Ming Zhang and Lulu Zhao

Department of Physics and Space Sciences, Florida Institute of Technology, 150 W. University Blvd., Melbourne, FL 32901, USA; [mzhang@fit.edu](mailto:mzhang@fit.edu)

Received 2017 June 6; revised 2017 August 13; accepted 2017 August 14; published 2017 September 7

## Abstract

Most solar energetic particles (SEPs) are produced in the corona. They propagate through complex coronal magnetic fields subject to scattering and diffusion across the averaged field lines by turbulence. We examine the behaviors of particle transport using a stochastic 3D focused transport simulation in a potential field source surface model of coronal magnetic field. The model is applied to an SEP event on 2010 February 7. We study three scenarios of particle injection at (i) the compact solar flare site, (ii) the coronal mass ejection (CME) shock, and (iii) the EUV wave near the surface. The majority of particles injected on open field lines are able to escape the corona. We found that none of our models can explain the observations of wide longitudinal SEP spread without perpendicular diffusion. If the perpendicular diffusion is about 10% of what is derived from the random walk of field lines at the rate of supergranular diffusion, particles injected at the compact solar flare site can spread to a wide range of longitude and latitude, very similar to the behavior of particles injected at a large CME shock. Stronger pitch-angle scattering results in a little more lateral spread by holding the particles in the corona for longer periods of time. Some injected particles eventually end up precipitating onto the solar surface. Even with a very small perpendicular diffusion, the pattern of the particle precipitation can be quite complicated depending on the detailed small-scale coronal magnetic field structures, which could be seen with future sensitive gamma-ray telescopes.

**Key words:** Sun: coronal mass ejections (CMEs) – Sun: flares – Sun: magnetic fields – Sun: particle emission

## 1. Introduction

An energetic event on the Sun, either a solar flare or a coronal mass ejection (CME), can produce high-energy particles up to a few GeV. Once these solar energetic particles (SEPs) are released from the Sun into the interplanetary space, they become a hazardous space weather component that could affect human lives and infrastructures in space as well as on the ground. Therefore, understanding the acceleration and transport of SEPs has a fundamental value to society. SEPs produced in the corona could also propagate down onto the solar surface, where they interact with the ambient gas and convert into gamma rays, a nonthermal component of high-energy electromagnetic radiation beyond the energy of thermal X-rays produced in solar flares. Studying the gamma rays from solar events can also lead to a better understanding of particle acceleration and transport in the solar corona.

Conventionally, there are two distinct acceleration mechanisms producing SEPs (Reames 1999). In gradual SEP events, particles are accelerated by shocks driven by CMEs, which can cover a large fraction of the entire solar surface. Gradual SEP events are large in lateral size and in intensity, and they last long periods of time with a typical elemental composition of the coronal plasma. In impulsive events, SEPs are accelerated by magnetic reconnection or turbulence in a compact region associated with solar flares. These events tend to be short and of low intensities, with more enhanced ratios of  ${}^3\text{He}/{}^4\text{He}$ ,  $\text{Fe}/\text{O}$ , and  $e/p$  than those typically seen in gradual events. The locations of flares associated with impulsive events are narrowly confined to the western limb of the solar disk (Reames 1999; Haggerty & Roelof 2002), suggesting that in impulsive events particles are injected from the Sun over a limited angular range around flares and follow the Parker spiral

magnetic field lines without much lateral propagation in the interplanetary space.

Multispacecraft measurements show that SEPs are often observed simultaneously over wide ranges of longitude, latitude, and radial distance. While the intensities at the beginning of the particle intensities observed at different locations are very (many orders of magnitude) different depending on the magnetic connectivity to the particle source on the Sun, they tend to approach a roughly uniform level (within a factor of 2–3) in a day or so and decay at the same rate afterward. Particles of different energies also decrease at roughly the same rate in the decay phase. The phenomenon was first reported by McKibben (1972), who used observations from Pioneer 6, Pioneer 7, and IMP-4 in the ecliptic. More such events have been studied using *Ulysses* at high heliographic latitudes (McKibben et al. 2001; Dalla et al. 2003; Zhang et al. 2003b). This phenomenon is commonly called the SEP reservoir effect (Roelof et al. 1992). The multipoint measurements with the identical twin spacecraft *STEREO-A* and *STEREO-B* at  $\sim 1$  au radial distance, in combination with near-Earth particle measurements (e.g., on *ACE*, *SOHO*, or *Wind*), have further improved our knowledge about the phenomenon (e.g., Dresing et al. 2012, 2014; Wiedenbeck et al. 2013; Lario et al. 2014, 2016, 2017). The wide longitudinal spread of SEPs from a CME event is not a total surprise, but the wide longitudinal spread of SEPs with the characteristics of impulsive events is unexpectedly observed in some events (Dresing et al. 2012; Wiedenbeck et al. 2013). Wiedenbeck et al. (2013) reported that  ${}^3\text{He}$  ions were detected by the two *STEREO* spacecraft and *ACE* on 2010 February 7, when a total range of  $\sim 136^\circ$  longitude was spanned by the three spacecraft. In some so-called circumsolar gradual SEP events (e.g., 2011 November 3, when *STEREO-A*, *STEREO-B*, and near-Earth spacecraft are roughly  $120^\circ$  apart from one another in longitude), SEPs with a strong outward

anisotropy are observed within 60 minutes from one another, which indicates that the particles are almost immediately injected near the Sun onto the field lines connecting to the spacecraft (Gómez-Herrero et al. 2015).

The observations of SEP spread over wide ranges of longitude and latitude have generated a lot of scientific interest. Many explanations have been proposed. The following are some examples. Broad sources of particles accelerated by coronal and interplanetary CME shocks may inject the particles into extended regions of the heliosphere (e.g., Cliver et al. 1995). The near-simultaneous widely separated solar eruptions could be another explanation for some SEP events (Schrijver et al. 2013). Complex magnetic field configurations in the corona and magnetic reconnection between open and closed field lines have also been suggested as mechanisms to spread particles to wide regions of the inner heliosphere (e.g., Richardson et al. 1991; Klein et al. 2008; Masson et al. 2013). Cross-field diffusion processes in the interplanetary space can allow particles injected from a narrow solar region to spread over a wide range of heliolongitudes (e.g., Zhang et al. 2009; Dröge et al. 2010). EUV waves propagating near the solar surface as a possible part of expanding CME may also accelerate SEPs and spread them over a large area on the Sun (Rouillard et al. 2012; Prise et al. 2014; Bućik et al. 2016).

This paper tries to extend the model of particle cross-field diffusion initially developed by Zhang et al. (2009). The model by Dröge et al. (2010) has the same mathematical formulation but uses a slightly different numerical implementation. The model has been successful in explaining a few key features of SEPs observed by spacecraft at multiple points in the heliosphere. For example, the phenomenon of an SEP reservoir can be naturally reproduced (Zhang et al. 2009; Qin et al. 2013; Qin & Wnag 2015). A number of other features that are commonly observed in SEPs are also reproduced (e.g., He et al. 2011; Wang et al. 2012, 2014; He & Wan 2017). Dröge et al. (2014, 2016) were able to fit multipoint observations in great detail using their interplanetary propagation model. The fits allowed them to derive particle diffusion coefficients and injection profiles together. In general, these models typically require a cross-field diffusion up to a few percent of particle parallel diffusion, which is quite reasonable from the theory of particle transport in turbulent interplanetary magnetic fields (e.g., Qin & Zhang 2014; Shalchi & Hussein 2014; and references therein). To fit spacecraft observations, the diffusion coefficients have to vary from one event to another and from one location to another, sometimes by a drastic amount (Dröge et al. 2016). However, even with typical levels of particle diffusion coefficients, particles can only slowly cross ambient magnetic field lines in the interplanetary space. It takes many hours before the onset of SEPs shows up on field lines that are tens of degrees away from the field lines where particles are injected (e.g., Zhang et al. 2009). The situation also leads to more delay in the time to the maximum particle intensity and no or little particle intensity anisotropy. The cross-field interplanetary transport cannot be used to explain SEP events with a prompt onset and a strong anti-sunward anisotropy. In order to explain the immediate SEP onset over a wide lateral range, SEP injection must cover a large area of the solar surface. The Dröge et al. (2014) model fitted the SEP electron observations by *STEREO-A*, *STEREO-B* and *ACE*, near Earth in the 2010 February 7 event. Their SEP source particle injection is assumed to have a Gaussian source injection profile

centered at the solar flare site of this event. A Gaussian standard deviation of  $\sigma_0 = 26^\circ$  angular size for the source injection is derived. Because most charged particle instruments on spacecraft are sensitive to particle intensity by several orders of magnitude lower than the SEP maximum intensity, the particle intensity at several  $\sigma_0$  angular distance away may still be seen as directly injected particles coming from the Sun along magnetic field lines with a strong anisotropy. In this sense, a Gaussian particle injection with a  $\sigma_0 = 26^\circ$  is still a quite broad source.

How can the SEP source be that wide before they escape from the corona? If it is a gradual event, in which particles are accelerated on a large CME shock front or extended EUV waves at the base, a nearly immediate particle injection on field lines over a large area on the Sun is not a surprise. However, the *STEREO* and *ACE* observations suggest that the 2010 February 7 SEP event has strong characteristics of impulsive events (Wiedenbeck et al. 2013; Dröge et al. 2014), which are rich in  $^3\text{He}$  and energetic electrons. Then the question is how the particles from the solar flare can spread already wide enough in the coronal magnetic fields. To undertake this investigation, we incorporate into our SEP propagation model a coronal magnetic field. In this paper, we use a potential field source surface (PFSS) model for the coronal magnetic field, which can be taken from, for example, the National Solar Observatory (NSO) GONG website. Effects of magnetic field turbulence are included in the form of particle pitch-angle scattering and perpendicular diffusion across the average magnetic field represented by the PFSS model. We inject particles somewhere in the corona according to assumed scenarios of particle acceleration. We use the focus transport equation to study how the injected particles propagate in the combined coronal and interplanetary magnetic fields and where they end up after a certain time. The injected particles either precipitate onto the solar surface or escape to the interplanetary space. The implications of the results will be given to shed light on the mechanisms of SEP release from the Sun or the production of nonthermal gamma-ray emissions in solar energetic events.

## 2. Model Description

To most energetic particles in the corona or interplanetary space, up to considerable high energies, their gyroradius is much smaller than the scale size of magnetic field inhomogeneity, and their gyroperiods are much shorter than magnetic field fluctuations. Up to a very good accuracy, the motion of particles in the ambient magnetic field can be described by an adiabatic approximation. In the presence of magnetic field turbulence, energetic particles experience pitch-angle scattering, and their guiding centers hop across the ambient magnetic field in a random fashion. The governing transport equation of particle distribution function  $f(t, \mathbf{r}, \mathbf{p}, \mu)$  as a function of time  $t$ , position  $\mathbf{r}$ , momentum  $\mathbf{p}$ , and pitch-angle cosine  $\mu$  can be written as

$$\frac{\partial f}{\partial t} = \nabla \cdot \boldsymbol{\kappa}_{\perp} \cdot \nabla f - (v\mu \hat{\mathbf{b}} + \mathbf{V} + \mathbf{V}_d) \cdot \nabla f + \frac{\partial}{\partial \mu} D_{\mu\mu} \frac{\partial f}{\partial \mu} - \frac{d\mu}{dt} \frac{\partial f}{\partial \mu} - \frac{dp}{dt} \frac{\partial f}{\partial p}, \quad (1)$$

where the terms on the right-hand side are cross-field spatial diffusion with a tensor  $\boldsymbol{\kappa}_{\perp}$ , streaming along the ambient or

average magnetic field direction  $\hat{\mathbf{b}}$  with particle speed  $v$  and pitch-angle cosine  $\mu$ , convection with the background plasma  $\mathbf{V}$ , particle gradient/curvature drift  $V_d$ , pitch-angle diffusion with a coefficient  $D_{\mu\mu}$ , focusing  $\frac{d\mu}{dt}$ , and adiabatic cooling  $dp/dt$ . In the adiabatic approximation, the drift velocity, focusing rate, and cooling rate may be calculated from the ambient magnetic field  $\mathbf{B} = B\hat{\mathbf{b}}$  and plasma velocity  $\mathbf{V}$  through

$$\begin{aligned} V_d = \frac{cpv}{qB} \left\{ \frac{1 - \mu^2}{2} \frac{\mathbf{B} \times \nabla B}{B^2} + \mu^2 \frac{\mathbf{B} \times [(\mathbf{B} \cdot \nabla) \mathbf{B}]}{B^3} \right. \\ \left. + \frac{1 - \mu^2}{2} \frac{\mathbf{B}(\mathbf{B} \cdot \nabla \times \mathbf{B})}{B^3} \right\}, \end{aligned} \quad (2)$$

$$\begin{aligned} \frac{d\mu}{dt} = -\frac{(1 - \mu^2)v}{2} \hat{\mathbf{b}} \cdot \nabla \ln B + \frac{\mu(1 - \mu^2)}{2} \\ \times (\nabla \cdot \mathbf{V} - 3\hat{\mathbf{b}}\hat{\mathbf{b}} : \nabla \mathbf{V}) - \frac{(1 - \mu^2)p}{v} (\mathbf{V} \cdot \nabla \mathbf{V}) \cdot \hat{\mathbf{b}}, \end{aligned} \quad (3)$$

$$\begin{aligned} \frac{dp}{dt} = -\left[ \frac{1 - \mu^2}{2} (\nabla \cdot \mathbf{V} - \hat{\mathbf{b}}\hat{\mathbf{b}} : \nabla \mathbf{V}) + \mu^2 \hat{\mathbf{b}}\hat{\mathbf{b}} : \nabla \mathbf{V} \right] \\ \times p - \frac{\mu p}{v} (\mathbf{V} \cdot \nabla \mathbf{V}) \cdot \hat{\mathbf{b}}. \end{aligned} \quad (4)$$

These terms in the first-order partial derivatives can be found in many previous publications (Northrop 1963; Roelof 1969; Skilling 1971; Ruffolo 1995; Isenberg 1997; Qin et al. 2004, 2006; Zhang 2006; Zuo et al. 2013). The second-order partial derivative terms represent the effects of magnetic field turbulence. The equation is truncated up to the diffusion term as approximated in the standard quasi-linear theory. In fact, even when the level of interplanetary magnetic field turbulence is sometimes comparable to or higher than the ambient magnetic field strength, many particle transport theories suggest that the particles will exhibit a diffusive transport behavior on timescales greater than the turbulence correlation time (Qin et al. 2002). Normally, there should be 10 independent Fokker–Planck diffusion coefficients in the diffusion tensor of the 5D phase space of  $\mathbf{r}$ ,  $p$ , and  $\mu$  (e.g., Schlickeiser 2002; Zhang 2006). Because the propagation speed of magnetic field turbulence, typically the Alfvén speed or fast-mode MHD wave speed, is much less than the speed of particles, stochastic particle momentum change by electric field fluctuations in the turbulence is much slower than the adiabatic cooling by the solar wind plasma, so all the diffusion terms related to  $p$  are neglected. With a steeply decreasing power spectrum of magnetic field turbulence in the solar wind, pitch-angle diffusion  $D_{\mu\mu}$  is mainly driven by the first resonance scattering, while the cross-field spatial diffusion  $\kappa_{\perp}$  is mainly driven by the random walk of field lines with approximately zero wavenumbers. If we assume that phases of magnetic field turbulence at different wavelengths are completely random or independent, pitch-angle scattering and cross-field spatial diffusion become uncorrelated, yielding zero off-diagonal diffusion elements in the diffusion tensor (Jokipii 1966). Therefore, only pitch-angle diffusion  $D_{\mu\mu}$  and cross-field diffusion  $\kappa_{\perp}$  are left in the particle transport Equation (1).

We commonly call Equation (1) the focus transport equation in 3D. The same equation was used in Zhang et al. (2009) and subsequent publications to investigate SEP propagation in the interplanetary space, where the ambient magnetic field and solar wind plasma can be described by the Parker model. In order to understand SEP transport in the solar corona, a more complicated model of the magnetic field and solar wind plasma has to be supplied.

### 2.1. Potential Field Source Surface Model

The coronal magnetic field is created by the solar dynamo. Its structure reflects the status of interaction between the solar interior and the Sun's surface and atmosphere. It can vary on timescales from minutes to the 11 yr solar cycle depending on spatial scale size. No fixed magnetic field model exists to describe the magnetic field in the corona. We have to depend on measurements at the time of events. Reliable magnetic field measurements using the magnetogram are only available to get the magnetic field vector in the photosphere. To get the structure of the entire coronal magnetic field, we have to compute 3D magnetic field models using the measured photospheric magnetic field as a boundary condition. A simplest commonly used model for the coronal magnetic field is the PFSS model. The model assumes that there is no electric current, which could be a good approximation, particularly on the large scale after the coronal plasma is completely relaxed of the Lorentz force.

PFSS magnetic field  $\mathbf{B}$  can be calculated from a scalar potential  $\Phi$  through  $\mathbf{B} = -\nabla\Phi$ , where  $\Phi$  expressed in a summation of spherical harmonics in polar coordinates  $r$ ,  $\theta$ ,  $\phi$  is (Altschuler & Newkirk 1969)

$$\begin{aligned} \Phi = R_0 \sum_{l=0}^{\infty} \sum_{m=0}^l \left[ l + 1 + l \left( \frac{R_0}{R_{ss}} \right)^{2l+1} \right]^{-1} \\ \times \left[ \left( \frac{R_0}{r} \right)^{l+1} - \left( \frac{R_0}{R_{ss}} \right)^{l+1} \left( \frac{r}{R_{ss}} \right)^l \right] \\ \times P_l^m(\cos \theta)(g_{lm} \cos m\phi + h_{lm} \sin m\phi), \end{aligned} \quad (5)$$

where  $P_l^m$  is the associated Legendre polynomial with a Gram–Schmidt orthonormalization.  $R_0 = 1 R_s$  (solar radius) is the lower boundary photosphere, and  $R_{ss}$  is the upper boundary at the solar wind source surface, where the magnetic field is assumed to be radial. Typically  $R_{ss} = 2.5 R_s$  from most data sources of the PFSS models. The spherical harmonic coefficients  $g_{lm}$  and  $h_{lm}$  are taken from fits to photospheric magnetogram measurements. We choose to use the coefficients from the NSO GONG website. Most of their outputs cut off beyond  $l_{\max} = 40$ .

The coronal magnetic field between  $R_0$  and  $R_{ss}$  rigidly corotates with the Sun. Because of this reason, we choose to set the spatial coordinates in a corotating reference frame. On the global scale, the structure of coronal magnetic field does not vary dramatically within a few days around a solar event. So we just use one set of spherical coefficients from the data provided by NSO. Typically it is the first available one immediately after the event on the Sun. We assume that plasma speed velocity is zero even on open field lines. This approximation will not affect the propagation of SEPs much because the plasma speed is very low compared to all other particle transport mechanisms.

A CME, particularly those of large sizes, can significantly change the coronal magnetic field configuration. Sometimes, the changes can be seen in the PFSS model by comparing the field maps before and after an eruption. Because of this reason, we choose to use the first one after the eruption. As the CME propagates out through the corona, the magnetic field around it may be continuously altered. This effect is probably hard to see in the PFSS model. Together with the constraint of available computation resource, we approximate the coronal magnetic field as a stationary field corotating with the Sun during the course of modeled SEP propagation.

## 2.2. Solar Wind and Magnetic Field

Above the radial distance  $R_{ss}$ , the solar wind speed becomes considerable. While the solar wind convection speed is still much lower than other transport speeds of SEPs, adiabatic cooling resulting from the divergence of solar wind velocity is the most important mechanism affecting particle momentum or energy. Because the distribution function of SEP source particles decreases steeply with particle momentum, a little momentum change can result in a large change of particle intensity. So it is important to include the effects of the solar wind, particularly in the interplanetary space.

There are many models for the solar wind that existed in the literature. For simplicity, we choose to use a crude model parameterized by Leblanc et al. (1998) in which the radial solar wind speed  $V_r$  and density  $n$  are approximated by

$$n = n_0 \left[ \left( \frac{r}{R_0} \right)^{-2} + k_4 \left( \frac{r}{R_0} \right)^{-4} + k_6 \left( \frac{r}{R_0} \right)^{-6} \right], \quad (6)$$

$$V_r = V_\infty \left[ 1 + k_4 \left( \frac{r}{R_0} \right)^{-2} + k_6 \left( \frac{r}{R_0} \right)^{-4} \right]^{-1}, \quad (7)$$

where  $k_4 = 12.4$  and  $k_6 = 242$  are taken from Leblanc et al. (1998). Figure 1 shows a radial profile of  $n$  and  $V_r$  in which  $n_0 = 8.4 \times 10^7 \text{ cm}^{-3}$  and  $V_\infty = 400 \text{ km s}^{-1}$  are used. With the plasma density, the Coulomb collision time for test particles can be estimated using the Lorentz collision model (e.g., Jackson 1999), where the Coulomb logarithm (Spitzer 1962) can be calculated, but it has a very weak dependence on the temperature profile assumed in Figure 1. For 100 keV electrons, the collision time is much longer than the particle residence time even at the base of open field lines. Therefore, we ignore the absorption of particles in the corona unless they hit the much denser photosphere, where we put it as an absorptive boundary.

In the corotating frame, the azimuthal speed of the solar wind should be zero at  $R_{ss}$  and become fully anti-corotating at infinity. We choose a linear approximation

$$V_\phi = -\Omega_s(r - R_{ss}) \sin \theta, \quad (8)$$

where  $\Omega_s$  is the angular speed of the Sun's rotation. The meridional plasma speed is  $V_\theta = 0$  everywhere in the solar wind. We use the Parker model for the magnetic field in the solar wind,

$$B_r = B_r(R_{ss}) \left( \frac{R_{ss}}{r} \right)^2, \quad B_\theta = 0, \quad \text{and} \quad B_\phi = B_r \frac{V_\phi}{V_r}, \quad (9)$$

where  $B_r(R_{ss})$  is the boundary value at  $r = R_{ss}$ , which is taken from the PFSS coronal magnetic field.

## 2.3. Diffusion Coefficients

Our model needs to be supplied with pitch-angle and perpendicular spatial diffusion coefficients. These coefficients are not directly measurable, so they have to be taken as free model parameters. We only have some theoretical guideline for choosing them. In reality, these coefficients could vary significantly from event to event or from one location to another. The paper will show how the scenarios of the diffusion coefficients can affect SEP propagation in the corona and interplanetary space.

For the pitch-angle diffusion coefficient we take the form of (Qin et al. 2005)

$$D_{\mu\mu} = D_0(r) p^{q-2} (1 - \mu^2) (|\mu|^{q-1} + h_0). \quad (10)$$

This simulates the results of the standard quasi-linear theory (e.g., Jokipii 1966; Schlickeiser 2002) of particle scattering in the magnetic field turbulence power-law spectrum of slope  $-q$ . For a Kolmogorov spectrum,  $q = 5/3$  in the inertial range of wavelength, but the slope becomes steeper in the dissipation range. The term containing  $|\mu|^{q-1}$  comes from the quasi-linear resonant scattering by magnetic field fluctuations

$$D_{\mu\mu}^{QL} = \frac{\pi^2 \Omega^2 (1 - \mu^2)}{B^2 v |\mu|} P_\perp(k_{\text{res}}) \quad \text{with} \quad k_{\text{res}} = \frac{\Omega}{v |\mu|}, \quad (11)$$

where  $\Omega$  is the particle gyroangularfrequency and  $P_\perp$  is the power spectral density of magnetic field turbulence in the direction transverse to the ambient magnetic field. The momentum dependence of  $D_{\mu\mu}$  comes from the theory of quasi-linear resonance scattering. Additional parameter  $h_0$  is to phenomenologically describe the enhancement of scattering through  $\mu = 0$  by either nonresonant scattering or nonlinear effects. Generally,  $h_0$  represents the uncertainty of  $\mu = 0$  when the guiding (at wavenumbers much lower than the resonant wavenumbers) magnetic field is varying or when there is a broadened resonance by a dynamic magnetic field turbulence. In the solar wind, it can vary significantly from 0.05 to 0.5 depending on the total amplitude of magnetic field fluctuations. For simplicity we set  $h_0 = 0.2$ . The result of our calculation is not very sensitive to  $h_0$  unless  $h_0 \ll 0.05$ .  $D_0(r)$  contains the spatial dependence of the pitch-angle diffusion coefficient due to the spatial variation of turbulence power or spectral shape.

After a sufficient amount of pitch-angle scattering, the particle transport along the ambient magnetic field with a varying pitch angle leads to a spatial diffusion with a parallel mean free path (Hasselmann & Wibberenz 1970)

$$\lambda_{||} = \frac{3v}{8} \int_{-1}^1 d\mu \frac{(1 - \mu^2)^2}{D_{\mu\mu}}. \quad (12)$$

Although the correspondence between particle mean free path and pitch-angle scattering can also be affected by the value of  $h_0$ , we generally use the value of particle mean free path to specify the intensity of particle pitch-angle scattering, which is mainly determined by the value of  $D_0$ .

The spatial dependence of  $D_0(r)$  is determined by the distribution of magnetic field turbulence. The calculation of the magnetic field turbulence spectrum everywhere in the corona or

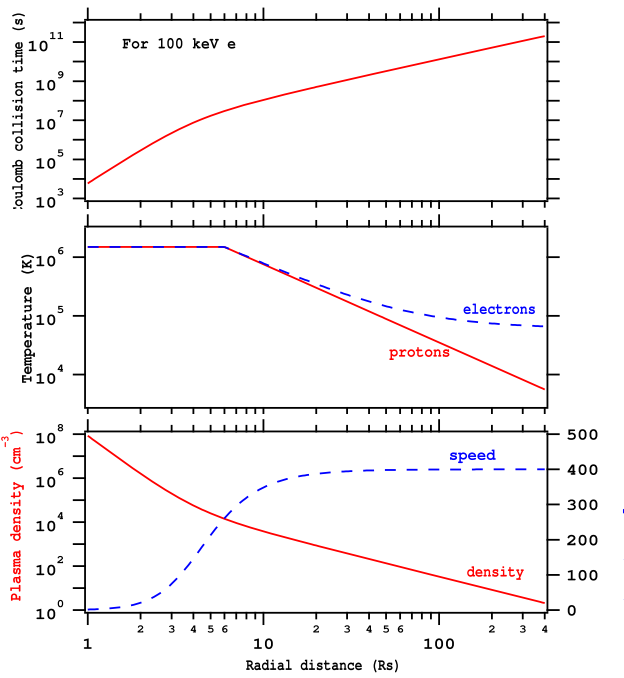


**Figure 1.** Solar wind model used in the calculation of SEP propagation. The density and radial speed (bottom) profiles are from Leblanc et al. (1998). The temperature (middle) is constructed from the theory of Meyer-Vernet & Issautier (1998). An estimated Coulomb collision time for 100 keV electrons (top) is derived using the test particle formulation in Jackson (1999).

in the solar wind requires complicated simulations using the reduced MHD or other theories. We borrow the results from earlier publications to estimate some general behaviors of  $D_0(r)$  as a function of  $r$ . According to Bieber et al. (1994), the radial mean free path,  $\lambda_r = \lambda_{\parallel} \cos^2 \psi$ , where  $\psi$  is the spiral angle of the Parker magnetic field to the radial direction, is nearly constant in the interplanetary space, where the solar wind plasma speed has almost reached its asymptotic value. Essentially all physics-based SEP interplanetary propagation model simulations employ this assumption (Zhang et al. 2009; Dröge et al. 2010, and in other subsequent publications). There is no previous calculation of particle parallel mean free path in the coronal magnetic field. We use the quasi-linear Equations (11) and (12) to make some estimations. Figure 2 shows the result of our own calculation with an input of the coronal magnetic field turbulence calculation done by Perez & Chandran (2013). Similar to that in the interplanetary space, the variation of the parallel mean free path in the corona is modest. The estimate of the parallel mean free path for 100 keV electrons is probably a little too low because we did not consider the reduced power spectral density of magnetic field turbulence in the dissipation range. On the other hand, since the coronal magnetic field can be greatly disturbed during an SEP event, an accurate assessment of the particle parallel mean free path is impossible. In our simulations below, we assume several scenarios (strong or weak scattering conditions) with a constant particle parallel mean free path in the corona up to  $20 R_s$ . The parallel mean free path in the interplanetary space can be quite different. We assume that the undisturbed interplanetary magnetic field starts at  $20 R_s$ . In all our simulations, we take a fixed  $\lambda_r = 20 R_s = 0.09$  au for the radial mean free path in the interplanetary space from Dröge et al. (2014), who found that their SEP interplanetary

propagation model can more or less fit the observations of 100 keV electrons from the 2010 February 7 SEP event with this value.

The spatial diffusion perpendicular to the ambient magnetic field  $\kappa_{\perp}$  could be due to the motion of particles following meandering or random walking magnetic field lines or due to particle hopping across the ambient magnetic field by the mechanisms of turbulent drift or scattering (Jokipii 1966). We usually use the ratio of perpendicular mean free path,  $\lambda_{\perp} = 3\kappa_{\perp}/v$ , to the parallel one,  $\lambda_{\perp}/\lambda_{\parallel}$ , to specify the strength of particle transport across field lines. When a particle source is small or they sample a small area of field lines such as those in small, low-energy impulsive SEP events, we will see that the particles are tightly confined in local magnetic flux tubes. Particle intensity drops out precipitously outside the flux tube (e.g., Mazur et al. 2000; Chollet & Giacalone 2011). The estimate of the  $\lambda_{\perp}/\lambda_{\parallel}$  ratio in this scenario is low,  $\sim 10^{-4}$  (Dröge et al. 2010). This low level of perpendicular diffusion comes from the particle's actual transport across the local actual magnetic field lines. If the particle presence occurs in an extended volume like cosmic rays, Jovian electrons, or SEPs in large gradual events, particle transport following the meandering field lines will result in a larger perpendicular diffusion with a  $\lambda_{\perp}/\lambda_{\parallel} \sim 10^{-2}$  (Potgieter 2000; Ferreira et al. 2001; Zhang et al. 2003a, 2007). The  $\lambda_{\perp}/\lambda_{\parallel}$  ratio can sometimes be greater than 1, as reported by Dwyer et al. (1997). Numerical simulations seem to indicate values of 0.02–0.05 for common levels of interplanetary magnetic field turbulence in the solar wind (e.g., Qin et al. 2002; Matthaeus et al. 2003). Because the purpose of this paper is to study the widespread presence of SEPs in the heliosphere, we focus on perpendicular transport on large scales due to the random walk of magnetic field lines.

The random walk of magnetic field lines in the heliosphere ultimately starts from the granular motion of plasma in the photosphere. The typical size for supergranules on the solar surface is about  $\delta x_0 = 3 \times 10^4$  km within a lifetime of about  $\delta t_0 = 24$  hr (Rieutord & Rincon 2010). We assume that the diffusion rate of magnetic field line footpoints on the solar surface is  $k_{gd} \langle \delta x_0^2 \rangle / \langle \delta t_0 \rangle$ , where  $k_{gd} \leq 1$  is a tunable factor specifying the strength of field line diffusion up to the full supergranule diffusion rate. As the magnetic field lines convect out with the solar wind plasma at the speed  $V$ , the diffusion rate of field line meandering along the field line  $z$  is

$$D_{FLRW} = \frac{\langle \delta z^2 \rangle}{\langle \delta z \rangle} = k_{gd} \frac{B_0}{B} \frac{\langle \delta x_0^2 \rangle}{V \langle \delta t_0 \rangle}, \quad (13)$$

where we have used the conservation of the mean magnetic field flux starting at the solar surface. For a population of particles moving along the field lines with an average parallel speed of  $v/2$ , their perpendicular diffusion coefficient is

$$\kappa_{\perp} = \frac{v}{2} D_{FLRW}, \quad (14)$$

which yields an energy- and species-independent particle perpendicular mean free path

$$\lambda_{\perp} = \frac{3k_{gd}}{2} \frac{B_0}{BV} \frac{\langle \delta x_0^2 \rangle}{\langle \delta t_0 \rangle}. \quad (15)$$

$\kappa_{\perp}$  could depend on particle pitch angle as a result of its speed of motion along the magnetic field; however, since particle pitch-angle scattering is typically much faster than perpendicular

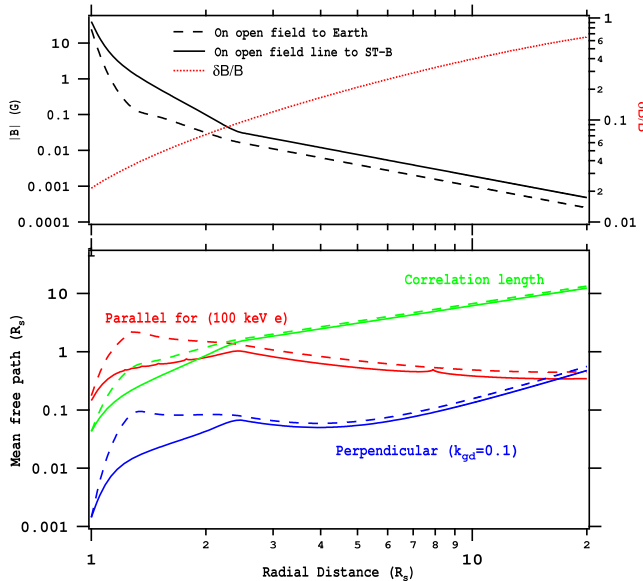


**Figure 2.** Estimates of particle parallel and perpendicular mean free paths as a function of radial distance along the two magnetic field lines connected to Earth and *STEREO-B* on 2010 February 7. The turbulence model for both the  $\delta B/B$  ratio and correlation length used for the calculation of the parallel mean free path is taken from Perez & Chandran (2013).

diffusion, the particle will sense an average parallel speed of  $v/2$  during each time step of perpendicular propagation. The average magnetic field on the solar surface  $B_0$  is  $\sim 1$  G. At 1 au, the magnetic field  $B$  is  $\sim 50 \mu\text{G}$  and plasma speed is  $400 \text{ km s}^{-1}$ . These parameters yield a  $\lambda_{\perp} = \sim 5 \times 10^{-3}$  au or  $\sim 1 R_s$  for the full strength of supergranule diffusion  $k_{\text{gd}} = 1$ , which turns out to be more than what is needed in most models of SEP propagation or cosmic-ray modulation calculations. This level of field line random walk is consistent with Giacalone & Jokipii (1999). On each specific field line, the variation of  $\lambda_{\perp}$  could change considerably as shown in Figure 2. On both field lines to *STEREO-B* and Earth shown in Figure 2, the  $B/B_0$  ratios are  $\sim 30$  times weaker than the value averaged over the entire surface. This results in an enhanced perpendicular transport in the vicinity of these lines.

### 3. Results

We now apply our model calculation to the 2010 February 7 SEP event. The event has been studied by several authors (e.g., Wiedenbeck et al. 2013; Dröge et al. 2014), so we only briefly summarize its major observational facts.

On 2010 February 7 *STEREO-A* was  $65^\circ$  in longitude ahead of spacecraft *ACE* at Earth and *STEREO-B* was behind Earth by  $71^\circ$ , all roughly at 1 au radial distance from the Sun. The solar wind speeds detected by the three spacecraft, *STEREO-A*, *ACE*, and *STEREO-B*, were approximately 450, 375, and  $500 \text{ km s}^{-1}$ , respectively. Assuming that the propagation of the solar wind from the Sun to 1 au is ballistic, we can locate the longitudes of their magnetic field line footpoints on the Sun at  $111^\circ$ ,  $61^\circ$ , and  $-20^\circ$  in the Heliocentric Earth Equatorial (HEEQ) coordinate system. The solar event on 2010 February 7 was produced by Active Region (AR) 11045. An M6.4 solar flare located at N21 E10 as viewed from Earth was observed to start at 02:20 and peak at 02:34. It was followed by a CME and an EUV wave as

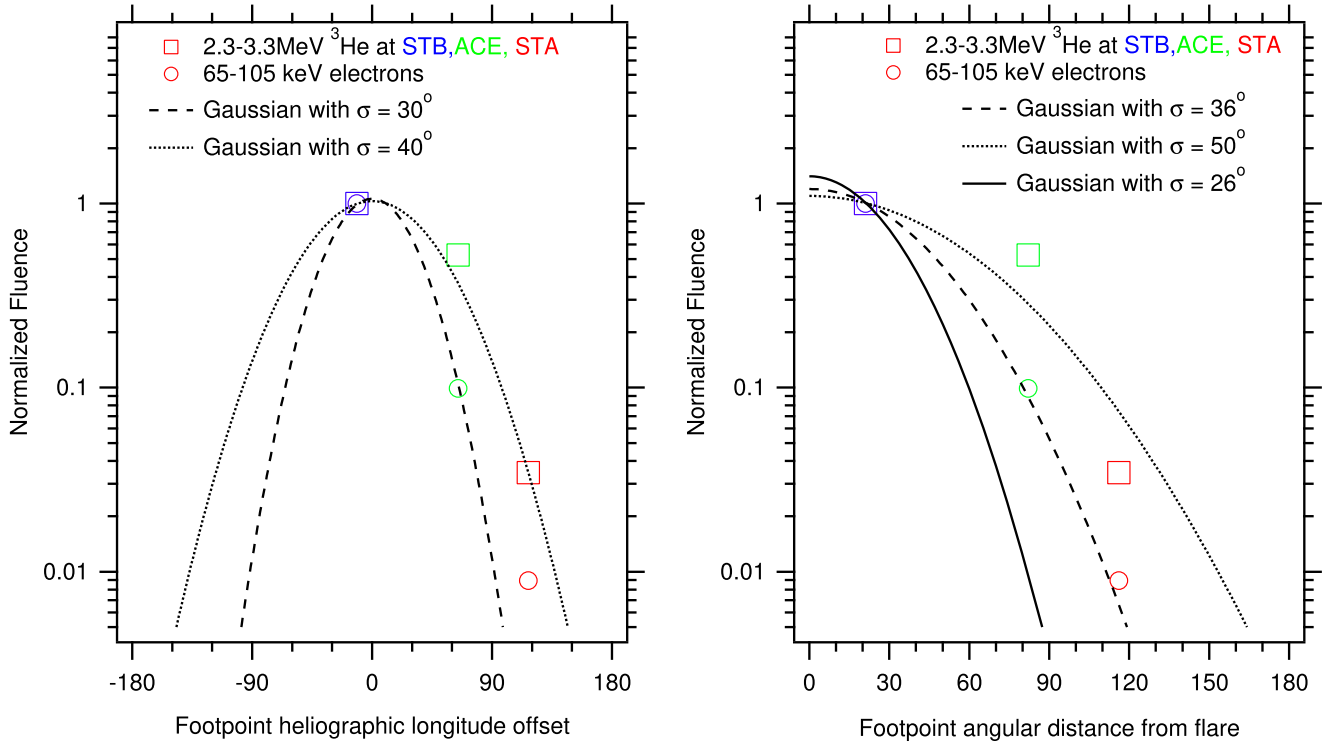
observed by the LASCO instrument on *SOHO*. The projected CME speed measured by *SOHO* was rather low,  $< 420 \text{ km s}^{-1}$ . Looking at the CME propagating nearly perpendicular to the line of sight, *STEREO-A* and *STEREO-B* confirmed that the CME was narrow ( $< 70^\circ$  in angular size) and slow ( $< \sim 570 \text{ km s}^{-1}$ ). The flare was accompanied by coronal and interplanetary type III radio bursts between 02:30 and 02:41. No type II burst radio signatures were detected either in the corona or in the interplanetary space, suggesting that there was no shock as the CME was too slow. The EUV wave was detected by all spacecraft at the three locations. It propagated mainly toward the southwest direction from the flare site. The EUV wave crossed the magnetic footprint of *STEREO-B*, which was only  $22^\circ$  away from the solar flare site. The EUV may have weakened substantially when it passed the magnetic footprint of *ACE*  $\sim 75^\circ$  away from the solar flare. It had disappeared well before it reached the magnetic footprint of *STEREO-A*  $121^\circ$  away from the solar flare.

All three spacecraft saw enhancement of SEPs from this event. Figure 3 shows the fluence of  $2.3\text{--}3.3 \text{ MeV } ^3\text{He}$  and  $65\text{--}105 \text{ keV}$  electrons as a function of longitudinal separation and angular distance from the solar flare of the magnetic field footprint. Gaussian curves with a few values of standard deviation are provided to demonstrate the size of the angular spread. Dröge et al. (2014) prescribe a source injection at the Sun using the Gaussian distribution with a standard deviation width of  $26^\circ$  (solid curve in the right panel of Figure 3). In the logarithmic vertical scale, the Gaussian distribution looks quite broad. The simulation by Dröge et al. (2014) showed that perpendicular diffusion of the particle in the interplanetary space is needed to spread the particles to the wider angular coverage of the observed SEP fluence. In the meantime, the three spacecraft detected a strong anti-sunward anisotropy in the fluxes of  $65\text{--}105 \text{ keV}$  electrons, suggesting that the particles were injected onto the field lines close to the Sun (Dröge et al. 2014).

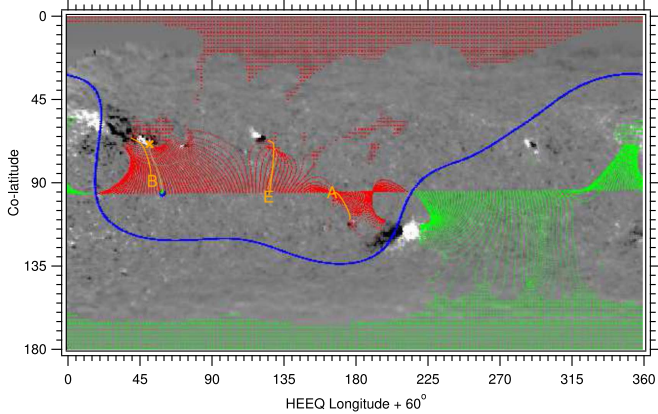
#### 3.1. Magnetic Structure of the Corona

Figure 4, taken from the online NSO GONG data archive, is a synoptic ecliptic field map as a function of HEEQ  $+60^\circ$  longitude and heliographic co-latitude. From now on, the longitude in all graphs is given in HEEQ longitude  $+60^\circ$ . The gray image is the photospheric magnetic field measurement at 5:54, the first GONG regular product after the solar flare/CME event. The red and green points are the projection of magnetic field lines connecting from the photosphere to open field lines in the ecliptic. The red points are downward field lines, and the green points are upward field lines. We have added the locations of magnetic footpoints to *STEREO-B* (B), Earth (E), and *STEREO-A* (A) and the projection (orange trace) of their magnetic field lines down onto the photosphere. Obviously, *STEREO-B* almost directly connects to the solar flare site that is represented by the orange dot, but Earth and *STEREO-A* are not directly connected to the solar flare.

The top panel of Figure 5 shows the footpoint location of all open field lines on the photosphere. Their loci roughly correspond to coronal holes. The background gray image is the calculated magnetic field strength on the photosphere. The red points are downward field lines, and the green points are upward field lines. We have drawn several circles (curves) of constant angular distances  $5^\circ$  (maroon),  $15^\circ$  (blue),  $45^\circ$  (teal), and  $75^\circ$  (yellow). These circles represent some possible sizes



**Figure 3.** Normalized fluence of 2.3–3.3 MeV  $^3\text{He}$  and 65–105 keV electrons as functions of longitude and angular distance from the solar flare at the magnetic footpoints to the spacecraft. Gaussian distributions with different levels of standard deviation are plotted to demonstrate the width of angular spread. The Gaussian curve in the solid line is the assumed source injection profile of the 65–105 keV electrons in the simulation by Dröge et al. (2014).



**Figure 4.** Synoptic ecliptic map of the coronal magnetic field from the NSO GONG database as a function of co-latitude and heliocentric Earth equatorial longitude  $+60^\circ$  at time 05:54 on 2010 February 7. The gray background image is the strength of the measured photospheric magnetic field. Green and red dots are projections of open magnetic field lines. The green dots are the outward-directed field, and red dots are inward field lines. The blue curve is the separatrix of the magnetic field of opposite polarities, which can eventually become a heliospheric current sheet in the interplanetary space. The projection of magnetic field lines connected to STEREO-B (B), Earth (E), and STEREO-A (A) is shown in orange. The orange cross is the location of the solar flare.

of SEP sources from different scenarios of the particle acceleration mechanism. The open field lines starting on the photosphere within the circles are mapped out. Their latitude-longitude locations on the solar wind source surface ( $R_{ss} = 2.5 R_s$ ) are shown in the bottom panel of Figure 5, where the absolute strength of the magnetic field from the PFSS model is displayed as the gray background image. The coverage areas of open field lines on the solar wind source surface have deformed and shifted significantly from their loci

on the photosphere. For example, the open field lines starting within  $5^\circ$  from the solar flare on the photosphere are mapped to an elongated maroon area in the bottom panel of Figure 5, which does not even cover the solar flare site. Projections of magnetic field lines to STEREO-B, Earth, and STEREO-A are shown in the orange traces. STEREO-B is very close to the open field lines directly connected to the solar flare. Earth is connected to an open field line region within  $75^\circ$  from the solar flare, but it is outside of the open field lines within  $45^\circ$ . STEREO-A is not directly connected in any of these cases of possible SEP source sizes.

After energetic particles are injected somewhere in the corona, they experience all effects of particle transport mechanisms. Even without cross-field transport mechanisms, i.e., perpendicular diffusion and gradient/curvature drift, the trajectories of particles are not just to follow magnetic field lines as we do in field line tracing, because particles injected with a finite pitch angle will experience adiabatic focusing or defocusing and some of them may get reflected by converging magnetic fields. The situation gets far more complicated when particle drift and perpendicular diffusion are included. We use a set of time-forward stochastic differential equations derived from the focus transport Equation (1),

$$dx = (v\mu \hat{b} + V + V_d + \nabla \cdot \kappa_\perp)dt + \sqrt{2\kappa_\perp} \cdot dw(t), \quad (16)$$

$$dp = \frac{dp}{dt} dt, \quad (17)$$

$$d\mu = \left[ \frac{d\mu}{dt} + \frac{\partial D_{\mu\mu}}{\partial \mu} \right] dt + \sqrt{2D_{\mu\mu}} dw(t), \quad (18)$$

to trace the guiding center, momentum, and pitch angle of energetic particles and study how they propagate in the corona

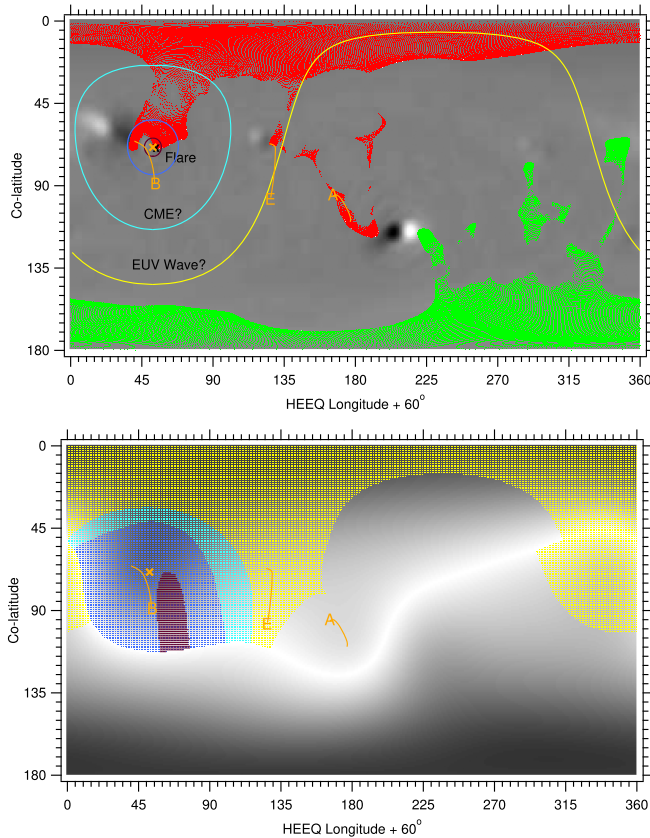


**Figure 5.** Top: calculated locations of all open field line footprints on the photosphere. The green dots are the outward-directed field, and red dots are inward field lines. The background gray image is the calculated magnetic field strength on the photosphere. The maroon, blue, teal, and yellow curves indicate circles of  $5^\circ$ ,  $15^\circ$ ,  $45^\circ$ , and  $75^\circ$  angular distance from the solar flare site (orange cross). Bottom: calculated footpoint locations on the solar wind source surface at  $2.5 R_s$  of open field lines within  $5^\circ$ ,  $15^\circ$ ,  $45^\circ$ , and  $75^\circ$  from the solar flare, with a background gray image showing the magnetic field strength at  $2.5 R_s$ . The projection of magnetic field lines connected to *STEREO-B* (B), Earth (E), and *STEREO-A* (A) is shown in orange color.

and interplanetary magnetic field. In Equation (16),  $w(t)$  is a 2D vector Wiener process, and the  $w(t)$  in Equation (18) is a scalar Wiener process. Since we are not certain about the source of SEPs in this event, we assume the following several scenarios with regard to it.

### 3.2. Injection at Compact Solar Flare Site

In this source injection scenario, we assume that energetic particles are injected in a compact region within  $5^\circ$  from the flare site. Since we do not look at the spectral evolution of particles, we just uniformly inject a monoenergetic nonthermal particle population of 100 keV electrons. The particles are injected  $0.05 R_s$  above the photosphere with an isotropic pitch-angle distribution. Since we do not even know whether the particles are produced on open or closed field lines, we provide calculations for both of these cases. First, we look at the propagation of particles injected on open field lines only with no perpendicular diffusion and a large parallel mean free path of  $5 R_s$  inside the corona up to a radial distance of  $20 R_s$  (Case 0A). Figure 6 shows the location and intensity of particles that have hit the photosphere, which we assume is an absorptive boundary. Notice that the intensity is given in  $\log_{10}$  scale, which tends to exaggerate weak emission sites compared to

imagery in the linear scale. Only 7.8% of particles end up precipitating down onto the photosphere in Case 0A. The small percentage of precipitation is mainly due to mirroring by the stronger magnetic field at lower altitudes. The locations of precipitation are confined to a single spot with open field lines. Figure 7 is the distribution histogram of particles as a function of residence time in the corona before they precipitate down onto the photosphere. There appear to be two populations of precipitating particles. The majority of particles in Case 0A precipitate down onto the photosphere directly within 0.015 minutes, and a very small tail distribution of long residence time contains particles that have gone through a sufficient amount of scattering in the corona and interplanetary space. Most (92.2%) of the injected particles on the open field line eventually escape to the interplanetary space. Figures 8 and 9 show the footpoint distribution of magnetic field lines on the solar wind source surface of  $2.5 R_s$  of the remaining particles in the outer corona and interplanetary space ( $> 2.5 R_s$ ). They are confined to the locus of open field lines without perpendicular diffusion in Case 0A. There is a little nonuniformity of particle intensity, mainly due to the different degrees of magnetic field tube expansion when it is mapped from  $1.05 R_s$  to  $2.5 R_s$ . The footpoint of the magnetic field line to *STEREO-B* is very close to the escaping particle source, but the magnetic footpoints to Earth and *STEREO-A* are far away. Figure 10 shows the distribution of particles as a function of radial distance at a few selected time intervals. In Case 0A, the parallel mean free path is set to  $5 R_s$  in the corona up to a radial distance of  $20 R_s$ . The radial mean free path in the interplanetary space is a constant at  $\lambda_r = 20 R_s$  or 0.09 au, which is roughly the same level as in the simulation by Dröge et al. (2014), and it is kept the same throughout all the simulations presented in the paper. The large mean free path in the corona allows the particles to leave the corona quickly. Within 3 minutes, half of the particles have already gone beyond  $20 R_s$ , and by 12 minutes essentially all of them have left the corona. Particles do not show up at  $215 R_s$  (1 au) until a much later time of 27 minutes. By 48 minutes, the peak particle intensity is still well inside  $215 R_s$ . If the coronal magnetic field is more disturbed with a much-decreased particle parallel mean free path of  $0.5 R_s$  (Case 0B), the longitudinal and latitudinal distributions of precipitating particles and escaping particles remain the same as in Case 0A. Only the percentage of precipitating particles increases to 8.7% (Figure 7). The increased precipitation occurs mostly through the scattering that results in more particles with a long residence time in the corona. The directly precipitating particle population shows few changes. The radial distributions of escaping particles with the smaller parallel mean free path in the corona are shown in Figure 10. Due to the small mean free path in the corona, most particles are not able to go beyond  $20 R_s$  within 48 minutes.

When the particle perpendicular diffusion is considered, the situations of particle precipitation and particle escape become more complicated. Cases 1–3 in Figure 6 show the distribution of precipitating particles on the photosphere. In these cases, particles are injected on open field lines within  $5^\circ$  from the solar flare site and  $0.05 R_s$  above the photosphere. With a finite perpendicular diffusion equal to  $k_{gd} = 0.1$  times the supergranular diffusion rate, particles can diffuse to closed field lines and eventually precipitate down onto the photosphere. The total percentage of particles precipitating on the photosphere has increased to 16% in Case 1. The intensity of particle

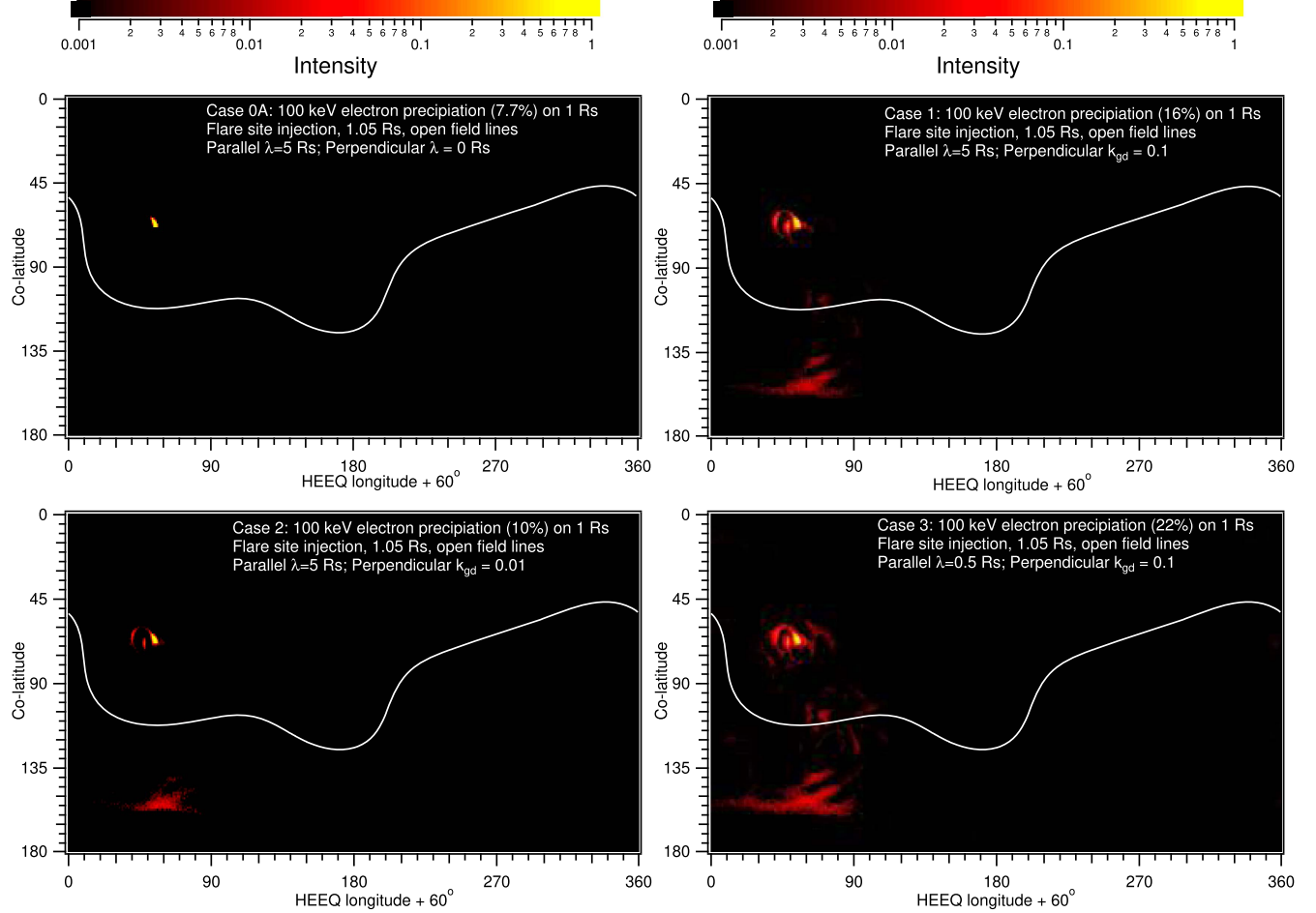


**Figure 6.** Intensity distributions of all precipitating particles in the  $\log_{10}$  scale on the solar surface. All particles are injected on open field lines  $0.05 R_s$  above the surface within  $5^\circ$  from solar flare center. Different levels of particle parallel and perpendicular mean free paths result in different patterns and intensities of precipitation. The curves are the separatrix of the magnetic field of opposite polarities.

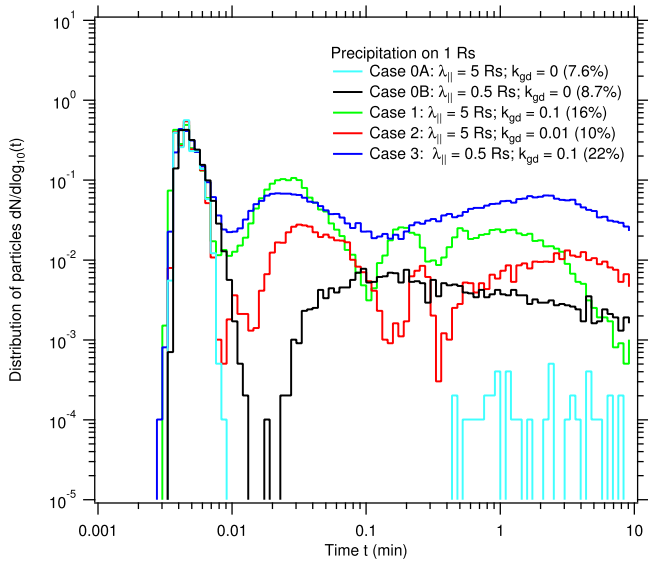


**Figure 7.** Normalized distribution of precipitating particles as a function of time since initial injection in equal  $\log_{10}$  spacing.

precipitation is strongest on open field lines with direct particle injection, but the precipitation on the footpoints of closed field lines could be visible with somewhat weaker intensities than the main site of open field lines. Figure 7 shows the distribution

of particle residence time between the injection and precipitation. The first and the strongest peak represents those particles that directly precipitate without much scattering or bounce. The subsequent peaks of Case 1 in Figure 7, due to multiple bounces on the closed field lines, are much weaker. Most particle precipitation has ended within 1 minute, meaning that after 1 minute essentially all the remaining (84%) particles in the corona will eventually escape to the interplanetary space. Figures 8–9 show the latitude–longitude distribution of the footprint of escaping particles remaining in the outer corona or interplanetary space at time intervals  $t = 12$  minutes and  $t = 48$  minutes after the initial injection. The image and its corresponding iso-intensity contours are in the  $\log_{10}$  scale with an arbitrary unit. Because of the perpendicular diffusion, the lateral spread of SEPs has increased substantially from the confined region of open field lines shown in Case 0A. The spread is particularly wide in weak magnetic field regions around the separatrix of opposite magnetic polarities, where  $\kappa_\perp$  is large. As the time progresses, the spread increases into the regions of weak particle presence. The distribution of escaping particles displays a diffusive nature, but it is not an exact Gaussian as assumed by Dröge et al. (2014). Taking a cut through the equator ( $90^\circ$  co-latitude), we get a distribution of particles as a function of longitude. Figure 11 shows the particle longitudinal distribution at five different time intervals. A Gaussian fit is made to each of them. Surprisingly, the

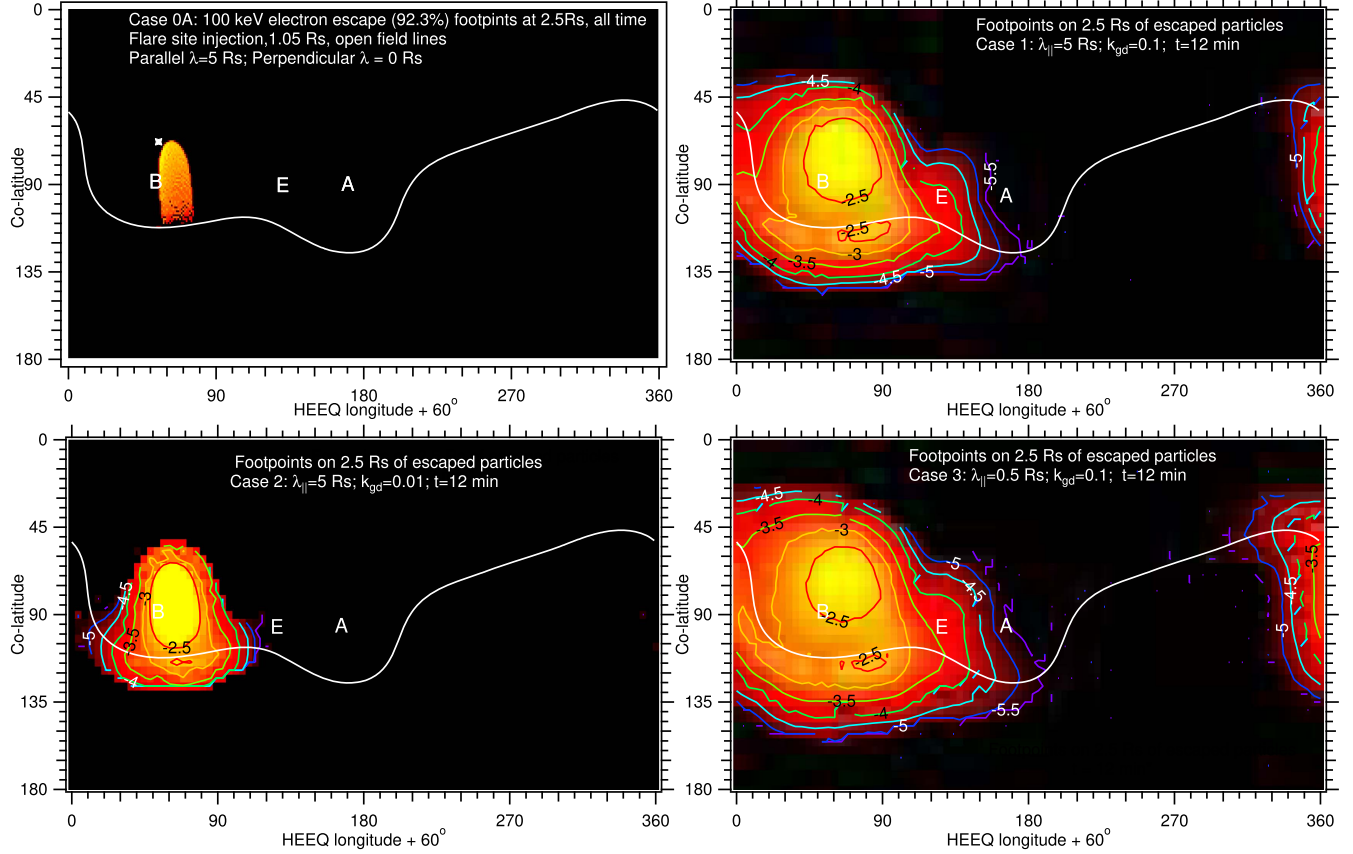


**Figure 8.** Distribution of the magnetic footpoint of escaping particles in the  $\log_{10}$  scale on the solar wind source surface  $2.5 R_s$  at  $t = 12$  minutes.

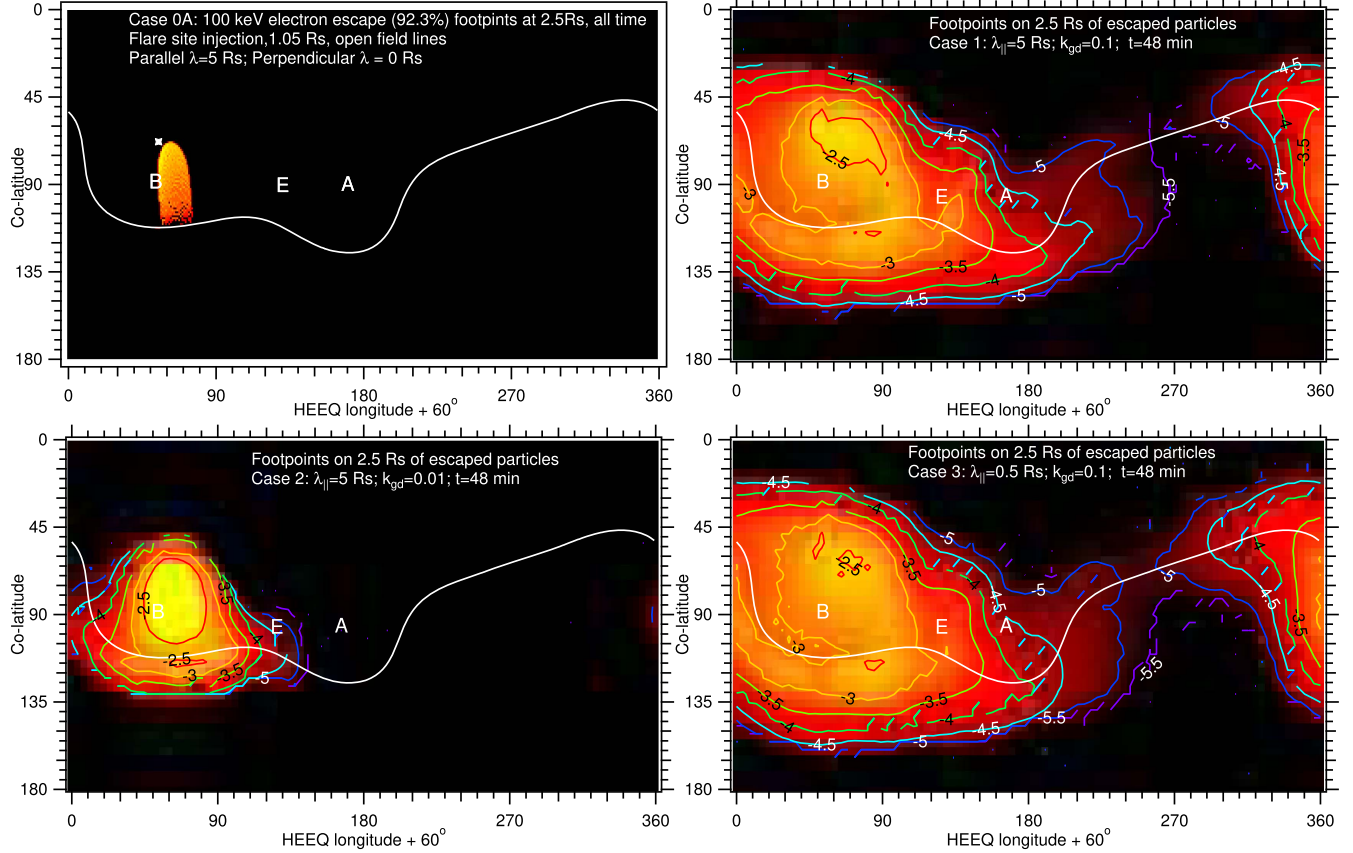


**Figure 9.** Distribution of the magnetic footpoint of escaping particles in the  $\log_{10}$  scale on the solar wind source surface  $2.5 R_s$  at  $t = 48$  minutes.

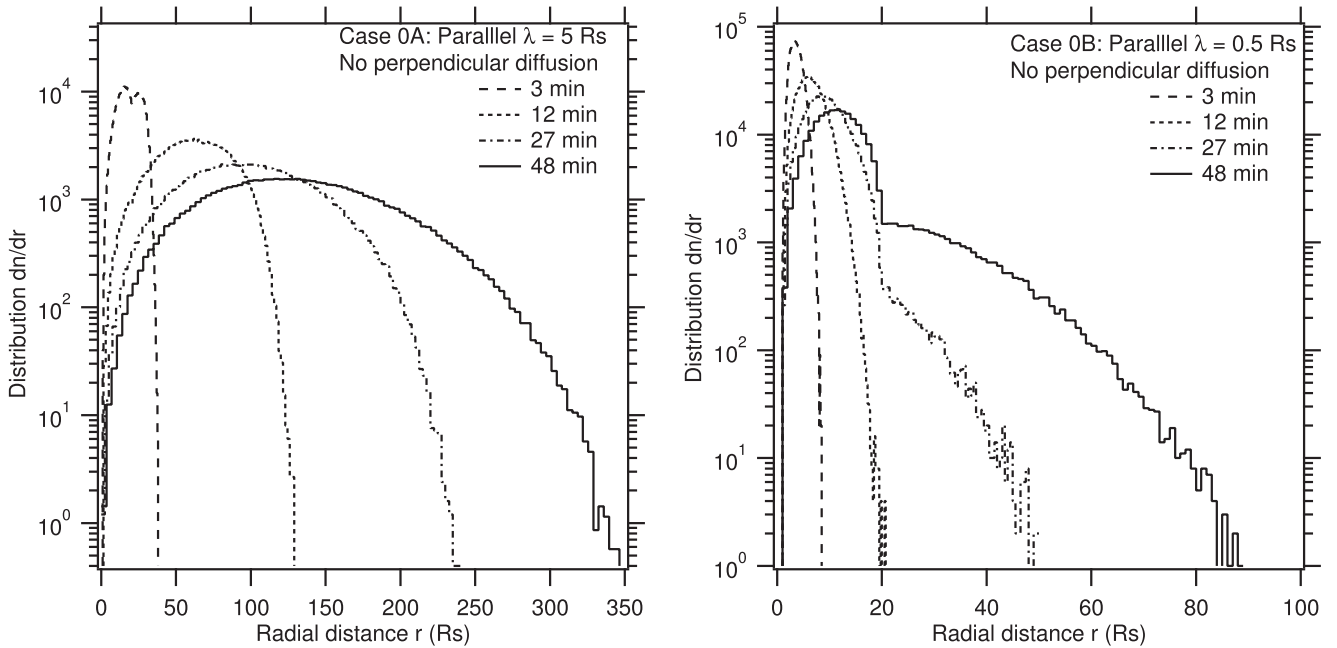


**Figure 10.** Radial distribution of escaping particles at four time intervals in Case 0A and in Case 0B with a reduced parallel mean free path inside the corona.

Gaussian curve can fit the core part of the distribution quite well. The standard deviation width of Gaussian distribution increases with time (Figure 12). Initially, the Gaussian width is  $\sim 10^\circ$ , approximately half the width of particle-filled open field lines on the solar wind source  $2.5 R_s$ . By 27 minutes, the Gaussian width has already exceeded  $26^\circ$  in Case 1, which is the number used as the source injection width in the simulation by Dröge et al. (2014). The time dependence of  $\sigma \propto t^{0.70}$  is close to the diffusive behavior of  $\sigma \propto \sqrt{t}$  from a point source. There is a non-Gaussian tail distribution in Figure 11. The tail becomes more and more prominent as the time increases. By 75 minutes, the tail has reached farther than  $210^\circ$  away from its core centered around the  $60^\circ$  longitude. The intensity of particles in the tail is just over a decade lower than that at the peak of the core distribution. It appears that the amount of longitudinal spread in this simulation with  $k_{gd} = 0.1$  times the supergranular diffusion in Case 1 is enough to explain the observations reported by Wiedenbeck et al. (2013) and Dröge et al. (2014). Figure 13 shows the distribution of escaping particle locations projected meridionally onto the equatorial  $x-y$  plane. It shows how wide the radial and longitudinal spreads are at  $t = 12$  minutes and  $t = 48$  minutes. The radial spread is the fastest on field lines that directly connect to particle source injection. Particles can spread laterally, but on field lines far away from the direct magnetic connection to particle source, the radial expansion is significantly delayed with a much lower particle density. This means that a spacecraft at 1 au will see a weak particle intensity and delayed arrival if it is not directly connected by the magnetic field to the source. Figure 14 shows the distribution of escaping particles as functions of remaining energy and the cosine of pitch angle to the anti-sunward direction of the local magnetic field line. The amount of energy loss from the initial injection energy of 100 keV is not that significant at the two time intervals of this case. The particle anisotropy directs outward from the Sun, and it gets small with time.

If somehow the random walk of magnetic field lines is not as strong, we are going to see the following results from a

simulation with  $k_{gd} = 0.01$  of Case 2. Figure 6 shows a smaller percentage (10%) of particle precipitation on the photosphere in Case 2. The main site that directly connects to the particle source on the open field lines remains the same intensity of particle precipitation (the first peak in Figure 7). Even with this small perpendicular diffusion, precipitation on closed field lines is still visible as multiple precipitation sites in Case 2 in Figure 6. The precipitation on the closed field lines is weaker in Case 2 than in Case 1 because the particles have a harder time diffusing into the closed field line regions. Figures 8 and 9 show the distribution of escaping particles at  $t = 12$  minutes and  $t = 48$  minutes. Figure 11 is the longitudinal distribution across the equator at five time intervals with their Gaussian fits. The core width increases slowly in proportion to the time (red curve in Figure 12), and such a speed of longitudinal spread is not fast enough to explain the measurements of SEPs observed by the two *STEREO* spacecraft and *ACE* at 1 au. The linear increase of the width is a result of the small spread from a relatively broader source.

If the coronal magnetic field is more disturbed, the particle parallel mean free path may be greatly reduced. Case 3 in Figure 6 shows the distribution of particle precipitation in a case with a small parallel mean free path of  $\lambda_{||} = 0.5 R_s$  in the corona within  $20 R_s$  radial distance. The percentage of particle precipitation has increased to 22%. This is because the strong scattering keeps the particles in the corona for longer periods of time so that they can find more chances to diffuse into the regions of the closed field lines. The main site of direct precipitation still remains the same intensity level. The other sites that anchor closed field lines, particularly those farther away from those open field lines with direct particle injection, experience more particle precipitation. The enhanced tail distribution of long residence time in Case 3 in Figure 7 is a result of these particles. Significant levels of particle precipitation can be seen to last over several minutes. Figures 8 and 9 show the distribution of magnetic footprints of escaping particles on the solar wind source surface at  $2.5 R_s$  in the  $\log_{10}$  scale for two time intervals, and Figure 11 is their longitudinal

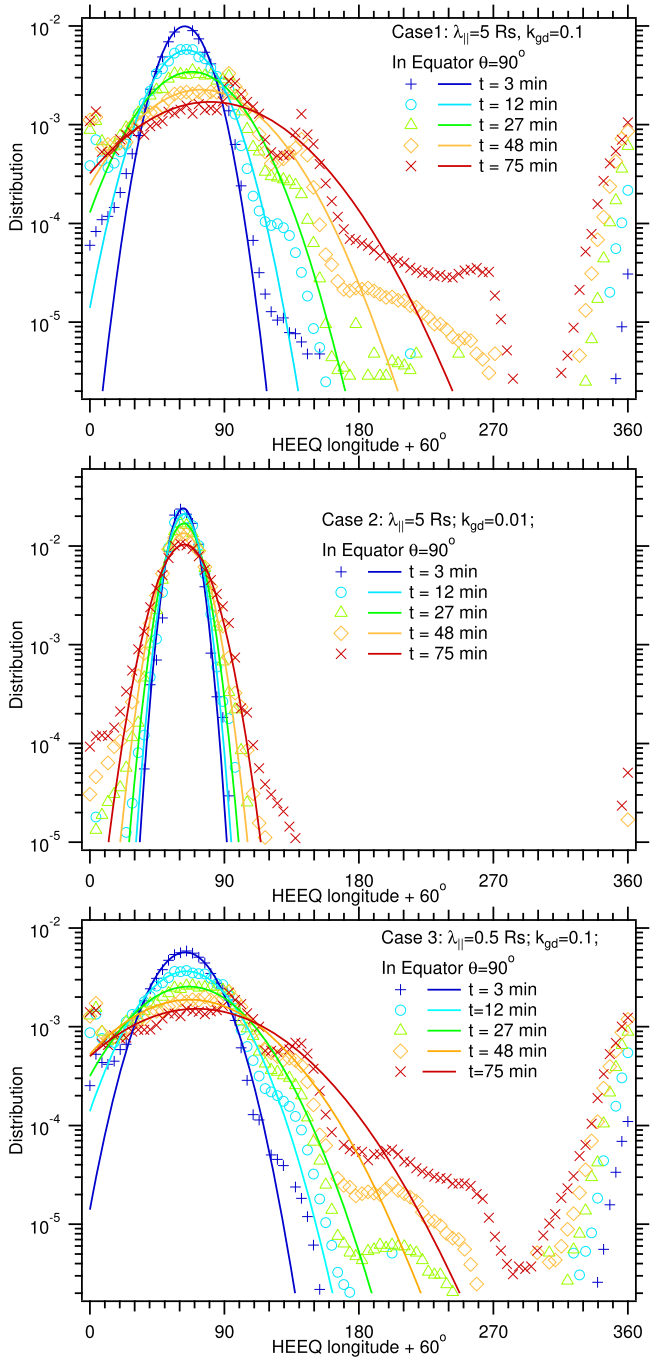


**Figure 11.** Longitudinal distribution of escaping particles in the equatorial plane with Gaussian fits.

cut in the equator with Gaussian fits. Apparently, the lateral spread of particles and development of a tail at large longitudinal separations in Case 3 have increased significantly from Case 1 with a longer parallel mean free path. The peak intensities in the core region of Case 3 are lower than in Case 1. Both effects result in a  $\sim 5^\circ$  wider Gaussian distribution in Case 3 than in Case 1 at all five time intervals after 3 minutes. The Gaussian width increases with time as  $\sigma \propto t^{0.54}$  in Case 3 of Figure 12, which is almost the same as the behavior  $\sigma \propto \sqrt{t}$  for particle diffusion from a point source. It further means that after 3 minutes the lateral size of spreading particles must have far exceeded the original size of particle source injection. Figure 13 shows the particle distribution projected along the

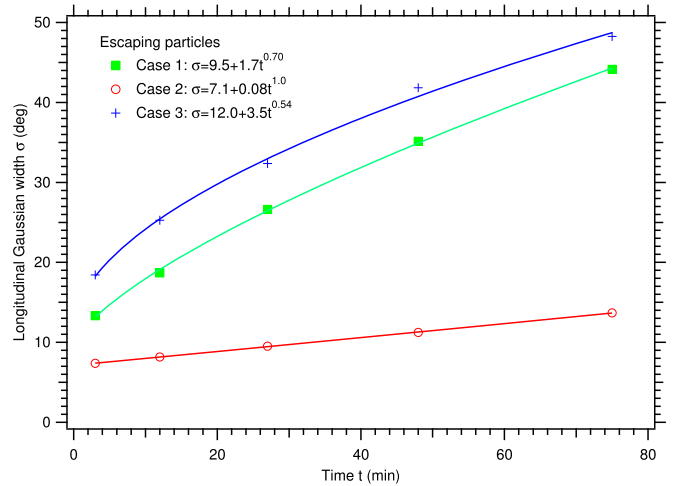


**Figure 12.** Width of Gaussian fits to the longitudinal distribution of escaping particles as a function of time.

meridian into the equatorial  $x-y$  plane. Compared to Case 1, the radial expansion has decreased owing to the smaller particle parallel mean free path in the corona  $< 20 R_s$ . The holding back of particles by scattering in the corona is more obvious at the early time ( $t = 12$  minutes). Once most of the particles have gotten out of the corona to beyond  $20 R_s$ , the radial expansion in the interplanetary space becomes faster. Nevertheless, even at  $t = 48$  minutes, there still appears to be a fraction of particles holding back in the corona as represented by the smallest red contour in Case 3 of Figure 13. Figure 14 shows the distribution of particles as functions of energy and the cosine of pitch angle to the outward field line direction. Because the particles have been held back near the Sun for longer periods of time in Case 3, the amount of energy loss in the solar wind has increased significantly, which can drastically reduce the particle intensity if the source particle spectrum decreases steeply with energy. The pitch-angle anisotropy in Case 3 is still increasing from  $t = 12$  minutes to  $t = 48$  minutes, indicating that during that time period the particles are still undergoing defocusing at fast rates near the Sun that exceed the rates of particle pitch-angle scattering.

If energetic particles are produced and injected on closed field lines, all of them will eventually precipitate down onto the photosphere if there is no perpendicular diffusion to get them to open field lines (Cases 0C and 0D). Figure 15 shows a distribution of precipitating particles from source particles injected  $0.05 R_s$  above the photosphere within  $5^\circ$  of the solar flare on closed field lines only. The particle precipitation appears at multiple sites, several of which have roughly equal intensities of particle precipitation. This is because the closed field lines at least anchor on two locations. In this case, due to the complicated magnetic field geometry around the solar flare, the closed field lines anchor on many separate sites. Figure 16 shows the time distribution of particles spent on the closed field lines before precipitation down onto the photosphere. The tail distribution of long residence time is much bigger, indicating that the particles have bounced back and forth inside the magnetic field arches many times. It appears that the level of particle scattering or parallel mean free path does not greatly affect the size of the tail distribution. With a longer mean free path or less pitch-angle scattering, the signatures of particle bouncing are more obvious, which is shown as the multiple peaks in the precipitation time distribution. If the particles can

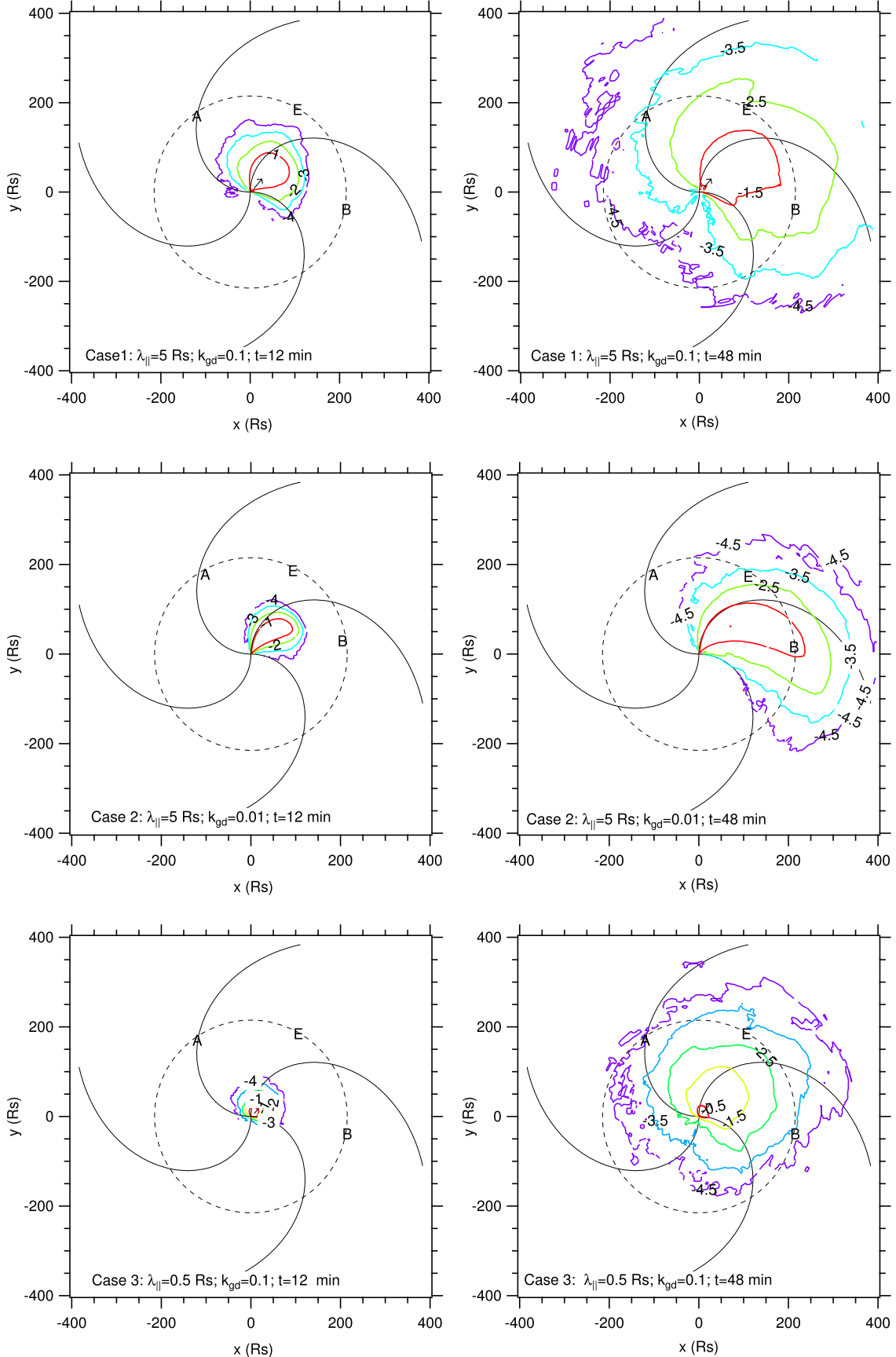


**Figure 13.** Distribution of escaping particles projected along the meridian to the equatorial  $x$ - $y$  plane. The locations of *STEREO-B*, Earth, and *STEREO-A* are labeled by the letters B, E, and A, respectively. The arrow indicates the direction of solar flare longitude.

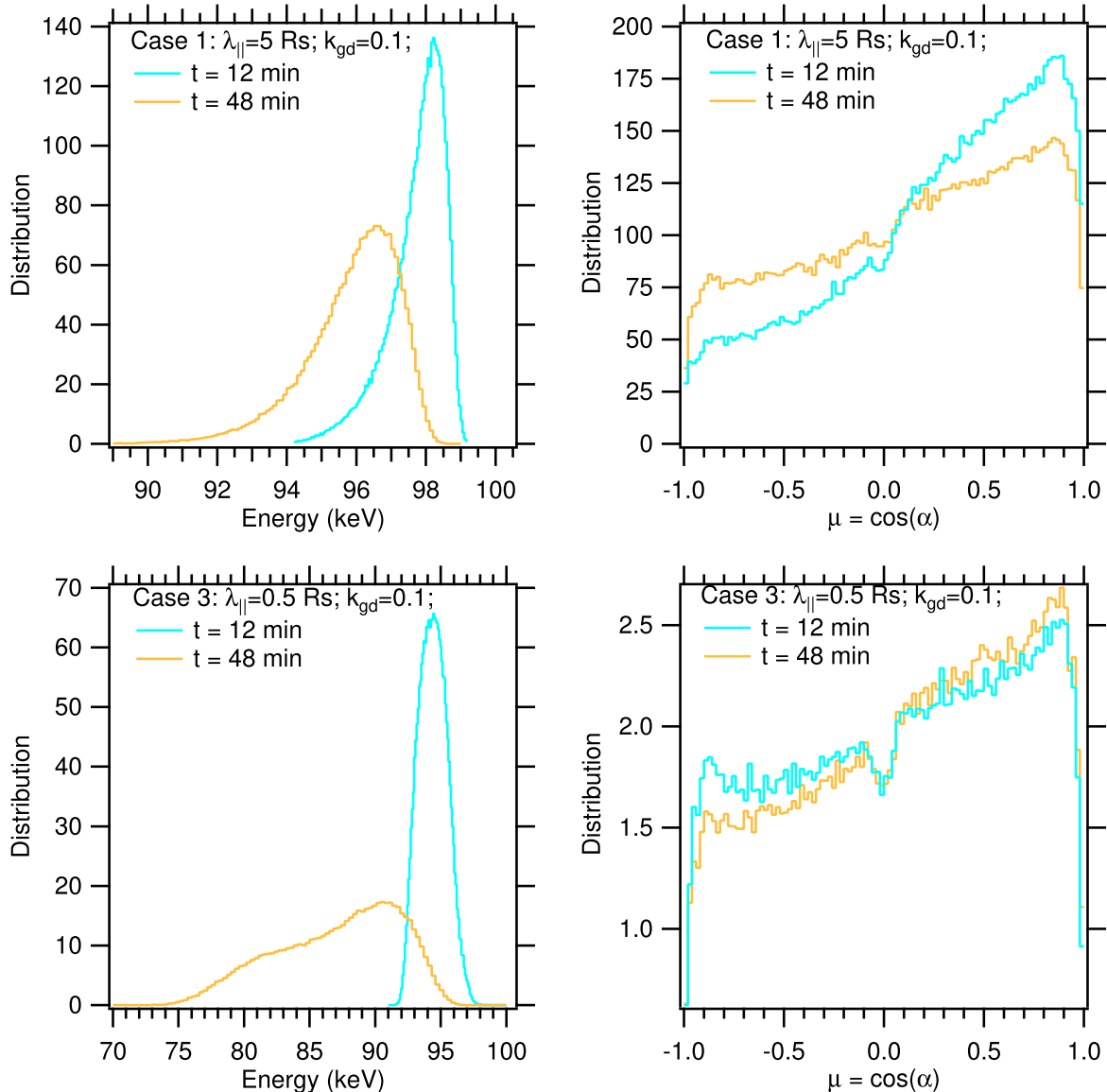


**Figure 14.** Distribution of escaping particles as functions of energy and cosine of pitch angle to the outward magnetic field line direction.

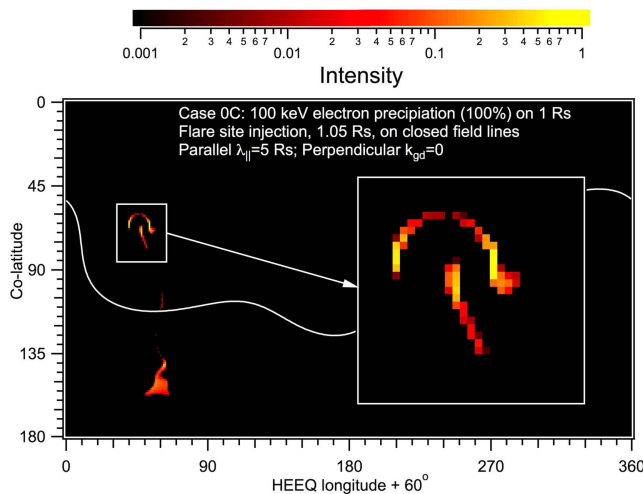


**Figure 15.** Intensity distributions of precipitating particles in the  $\log_{10}$  scale on the solar surface, with the inset showing a magnified profile of precipitation around the solar flare. All particles are injected on closed field lines  $0.05 R_s$  above the surface within  $5^\circ$  from the solar flare center.

convert into gamma rays efficiently, we will see emissions in addition to the solar flare site, and the emission intensity at the conjugate anchoring site is not too much weaker than the main site. This phenomenon has never been observed by gamma-ray observations, suggesting that it is unlikely that energetic particles are produced and injected on closed field lines. This is perhaps expected because particle acceleration occurring on closed field lines will suffer heavier particle loss owing to precipitation on both ends. From now on, we will only discuss cases in which particles are produced and injected on open field lines.

### 3.3. Injection at CME

There is a possibility that the CME of the 2010 February 7 event can accelerate particles despite the fact that the CME speed is too slow to drive a shock. We assume that particles are only produced and injected uniformly on open field lines within an angular distance of  $45^\circ$  from the solar flare site and particle injection at some fixed radial distances ( $1.5 R_s$  in Cases 4–6 and  $2.5 R_s$  in Case 7). In the following, we present the results of our

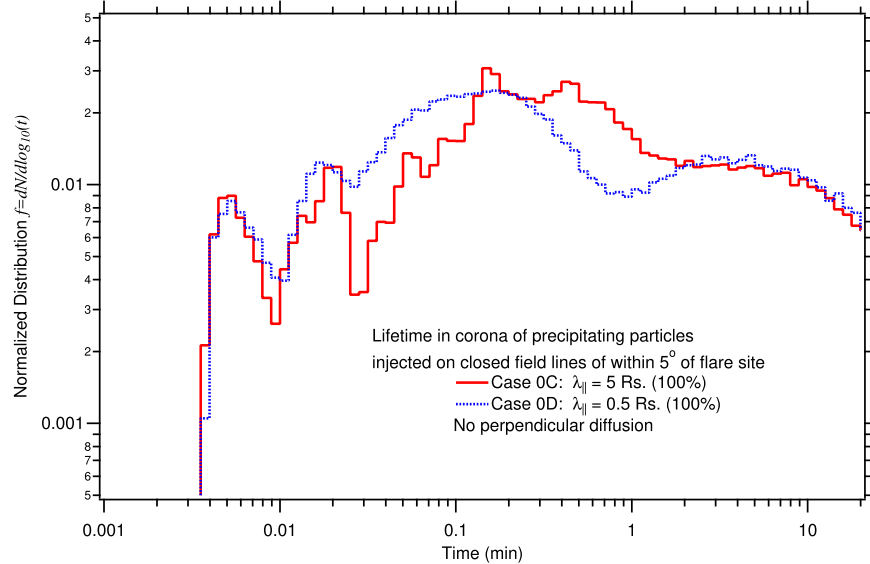


**Figure 16.** Distribution of precipitating particles as a function of time since initial injection. All particles are injected on closed field lines within  $5^\circ$  of the flare site.

calculations using several scenarios of particle transport coefficients in the corona.

In Case 4, perpendicular diffusion is set to zero. Figure 17 shows the distribution of precipitating particles on the photosphere. Only 1.9% of particles injected end up precipitating down onto the photosphere. This is mainly because of the height of particle injection, where the loss cone size is smaller owing to a weaker magnetic field. The locations of particle precipitation spread over all open field line regions within the CME coverage. Figure 18 shows the time distribution of all precipitating particles. The first peaks represent prompt particle precipitation. This is much larger than the second peak in Case 4. Figures 19 and 20 show the latitude–longitude distribution of escaping particles at two time intervals. The particles in Case 4 are confined to the regions of open field lines connected to the CME. Although there is a nonradial evolution of magnetic field from  $1.5 R_s$  to  $2.5 R_s$ , the mapping of the magnetic field from the CME does not change the coverage location and size very much, mainly because there is no particle injection on closed field lines on the CME. Figure 21 shows the distribution of particle locations projected on the equatorial  $x$ – $y$  plane at  $t = 12$  minutes and  $t = 48$  minutes.

If we allow perpendicular diffusion in Case 5, Figure 17 shows the distribution of precipitating particles on the photosphere. The percentage of particle precipitation has increased from Case 4, all of which is in the long-duration tail (Figure 18). Particle precipitation occurs over widely distributed regions of both open and closed field lines. Figures 19 and 20 show the latitude–longitude distribution of the magnetic footprint of escaping particles on the solar wind source surface  $2.5 R_s$ . Compared to Case 1 of particle injection at the compact solar flare site, the spread of particles is quite similar, except the core is a little wider. Figure 22 shows a longitudinal cut in the equator at five time intervals and with a Gaussian fit to the core. It can be seen that a non-Gaussian tail develops far away from the directly connected field lines. The projected distribution in the equatorial plane is shown in Case 5 of Figure 21. At  $t = 48$  minutes, the low-intensity contours have already covered the entire  $360^\circ$  longitude, while high-intensity contours of particles are more concentrated near the field lines directly connected to the CME particle source.

Case 6 presents a reduced parallel mean free path in the corona. Case 6 in Figure 17 shows the distribution of precipitating particles on the photosphere. The percentage of precipitating particles has increased to 13%. Its long-duration tail grows bigger in Figure 18. The precipitation occurs over more widely distributed regions on the photosphere, which cover much larger areas than the CME. The latitude–longitude distribution of escaping particles and its equatorial cuts are displayed in Figures 19, 20, and 22. The lateral spread is slightly increased with a reduced parallel mean free path. Case 6 in Figure 21 shows the distribution of particles projected onto the equatorial  $x$ – $y$  plane. The longitudinal spread of low-intensity particle contours is more extensive (closer to circular shape), while the radial expansion is greatly reduced from Case 5.

In Case 7, particles are injected with  $45^\circ$  angular distance from the solar flare at  $2.5 R_s$  radial distance, where the CME is already in the radial magnetic field of the solar wind. Case 7 in Figure 17 shows the distribution of precipitating particles on the photosphere. The particle precipitation is widely spread, but the intensity becomes low because only  $\sim 1.1\%$  of particles are injected or scattered into the loss cone from this high altitude. The black curve in Figure 18 demonstrates the time distribution of particle precipitation. The first peak represents particles precipitating down onto the photosphere without much scattering, and the long-duration tail contains particles that get onto the photosphere through scattering or perpendicular diffusion. Nearly all (99%) particles injected at this high-altitude CME eventually escape to the interplanetary space. Like in Case 5, with the perpendicular diffusion, the lateral spread of particles in Case 7 is wide and fast, as shown in Figure 22, where we show a longitudinal cut of particle distribution in the equator.

### 3.4. Injection in EUV Wave

There is a possibility that the EUV wave observed in this event can accelerate particles. Although the observable part of the EUV wave is on the solar surface, we expect that particles can only be accelerated to high energies at high enough altitude, where the atmospheric particle density has become

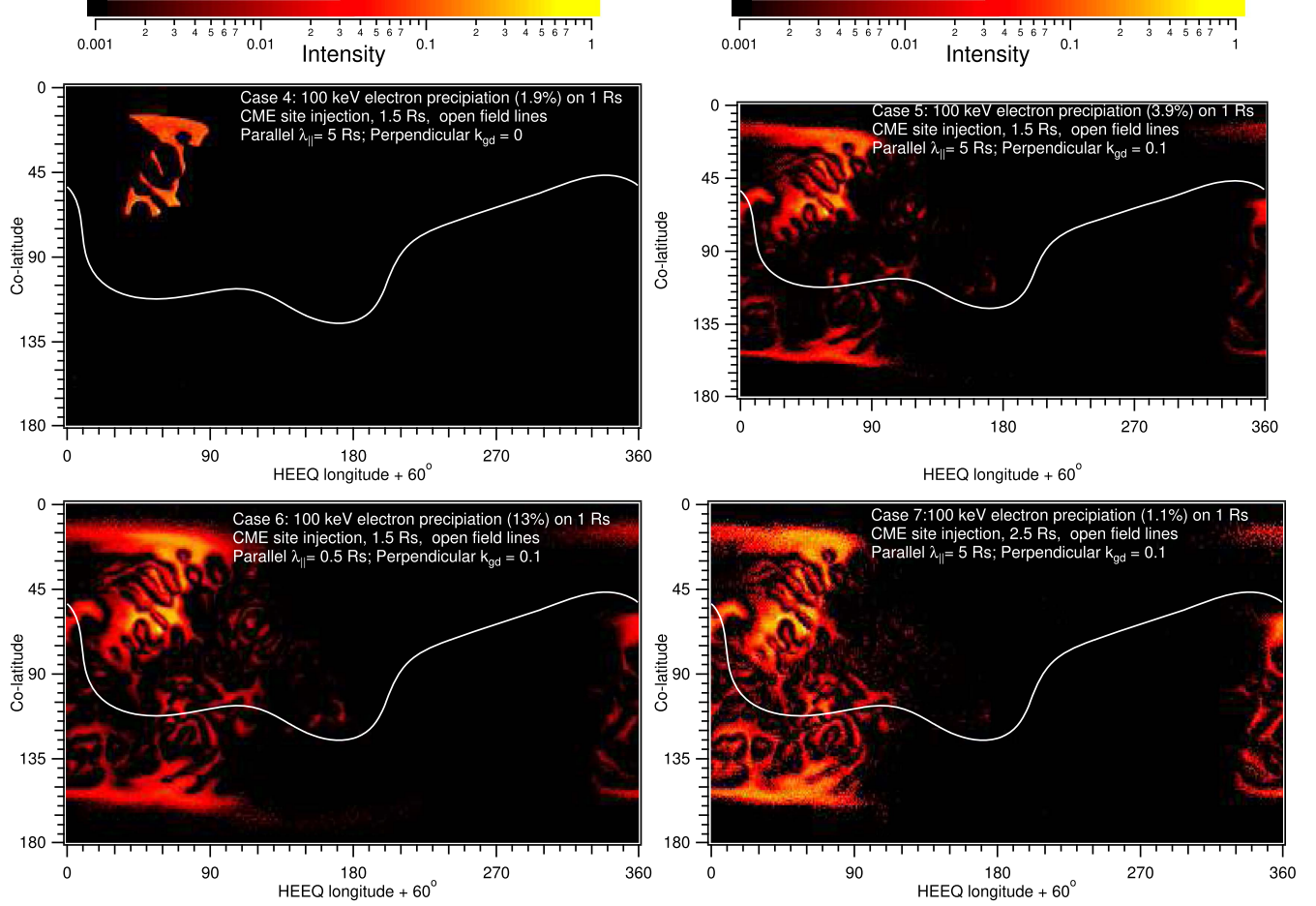


**Figure 17.** Distribution of precipitating particle intensity on the solar surface. Particles are injected on open field lines at the CME shock within  $45^\circ$  of the flare site.

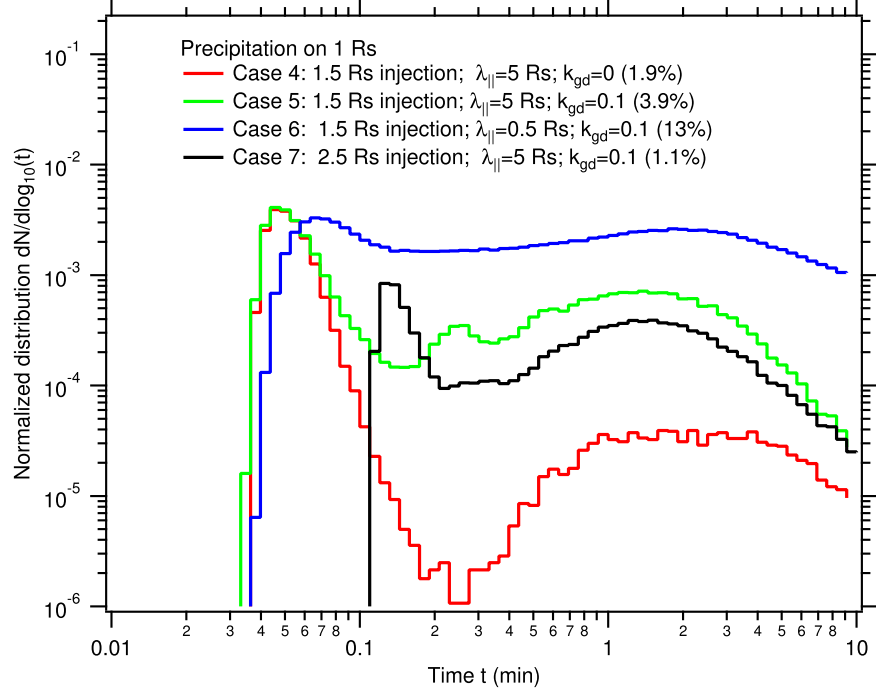


**Figure 18.** Distribution of precipitating particles as a function of time since initial injection in equal  $\log_{10}$  spacing. Particles are injected on open field lines at the CME shock within  $45^\circ$  of the flare site.

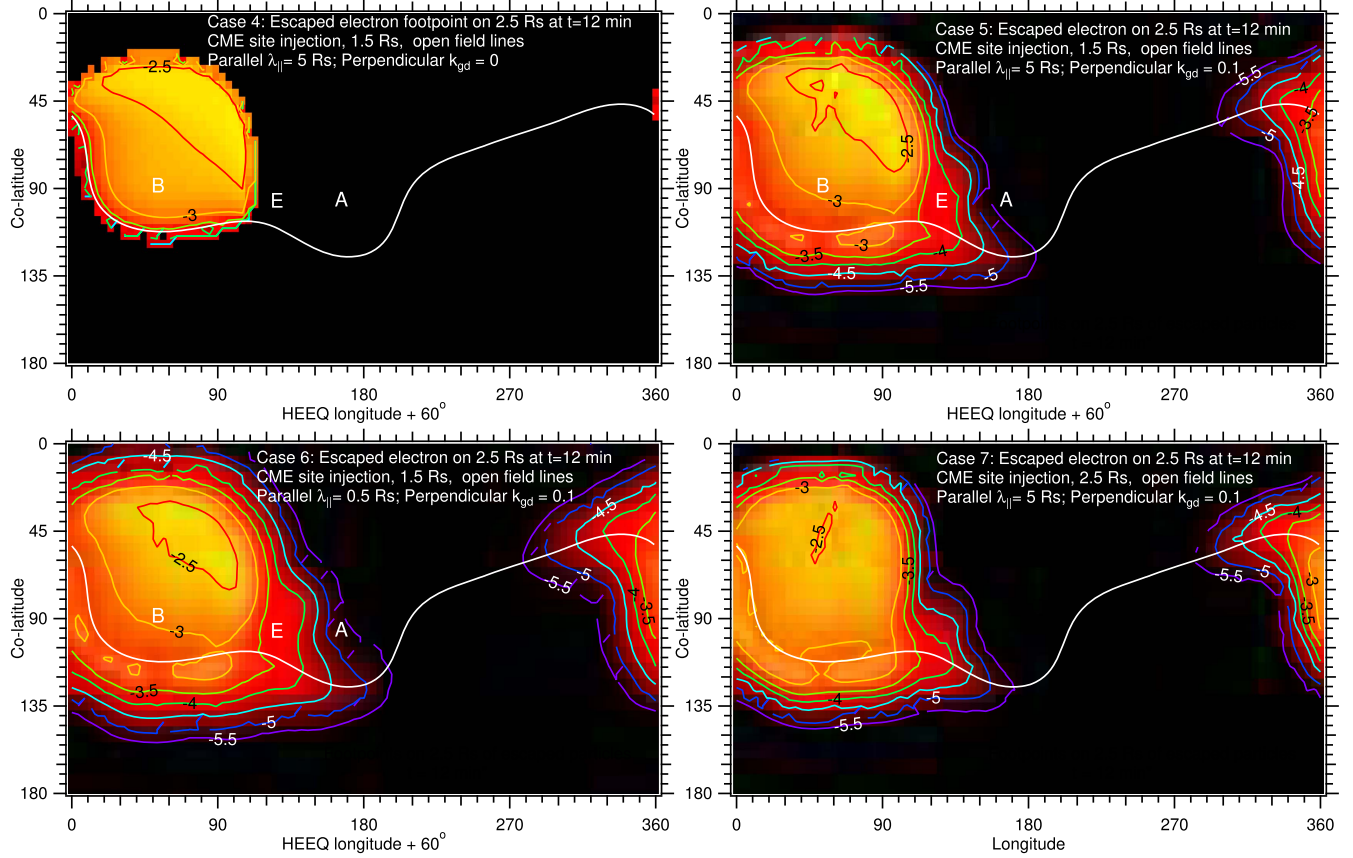


Figure 19. Distribution of the magnetic footpoint of escaping particles in the  $\log_{10}$  scale on the solar wind source surface  $2.5 R_s$ .

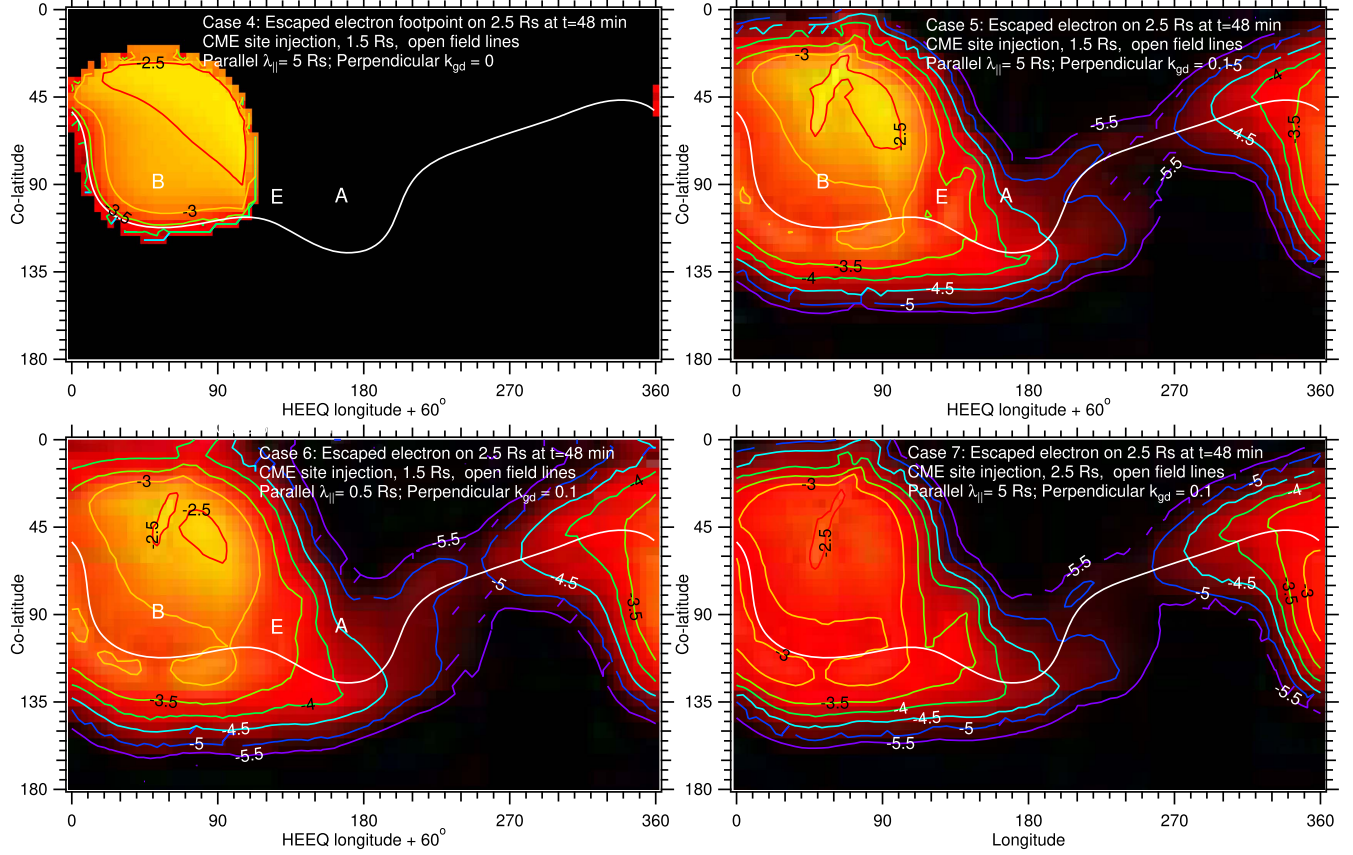
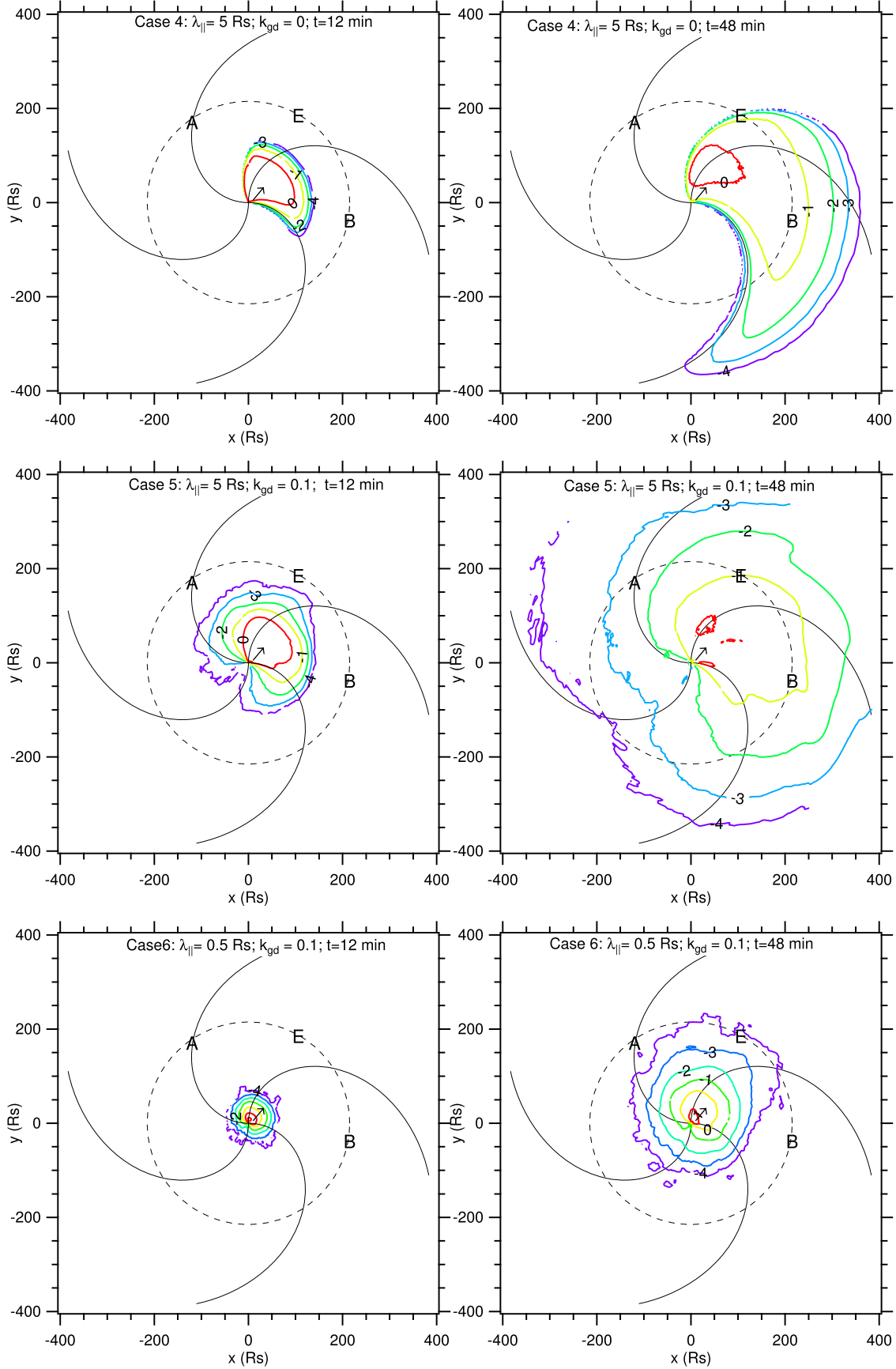
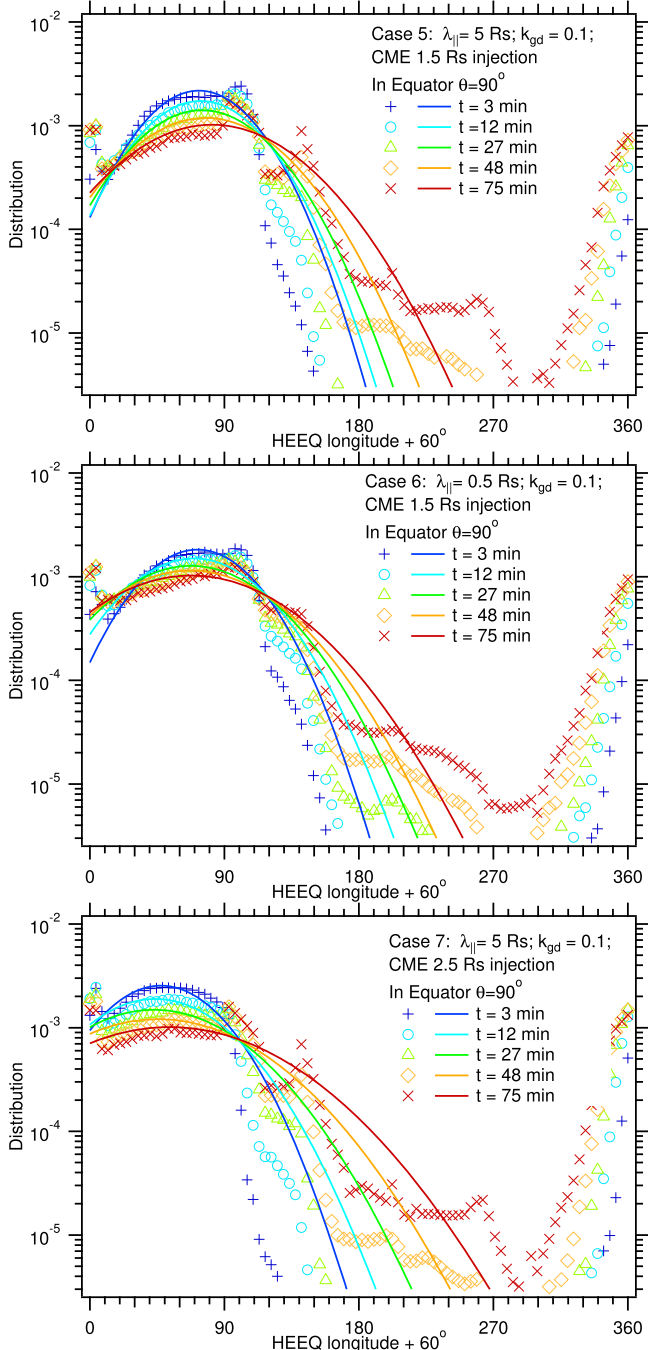


Figure 20. Distribution of the magnetic footpoint of escaping particles in the  $\log_{10}$  scale on the solar wind source surface  $2.5 R_s$ .



**Figure 21.** Distribution of escaping particles projected along the meridian to the equatorial  $x$ - $y$  plane. The locations of *STEREO-B*, Earth, and *STEREO-A* are labeled by the letters B, E, and A, respectively. The arrow indicates the direction of solar flare longitude.



**Figure 22.** Longitudinal distribution of escaping particles in the equatorial plane with Gaussian fits to the core.

thin enough to avoid collisional loss. Let us assume that energetic particles are uniformly produced and injected  $0.05 R_s$  above the photosphere over the area of open field lines covered by the EUV waves up to  $75^\circ$  from the solar flare site. Case 8 has a finite perpendicular diffusion equal to  $k_{gd} = 0.1$  times the full supergranular diffusion and a particle mean free path of  $5 R_s$  in the coronal magnetic fields. Figure 23 shows the distribution of precipitating particles from the EUV wave. The precipitation covers a wider area than in Case 6, mainly because the EUV of  $75^\circ$  angular size extends into the polar field lines. About 26% of particles eventually end up precipitating onto the photosphere. (Note that here particles

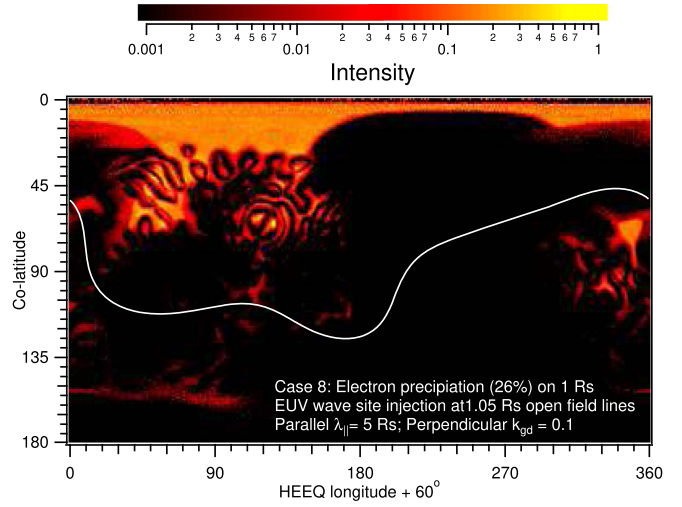


**Figure 23.** Distribution of precipitating particle intensity on the solar surface.

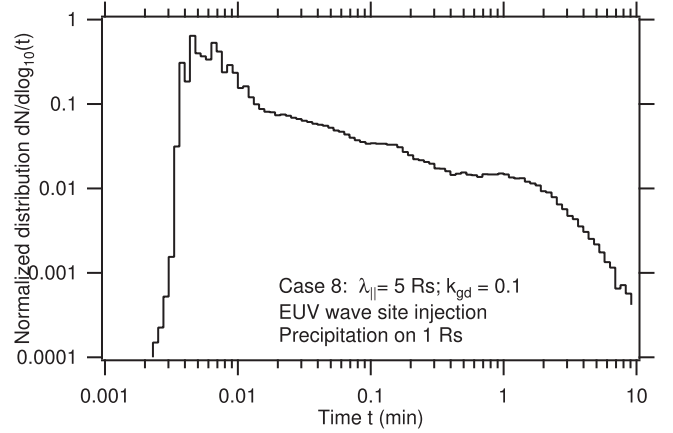


**Figure 24.** Distribution of precipitating particles as a function of time since initial injection in equal  $\log_{10}$  spacing.

are only injected on the open field lines, and if energetic particles are also produced on closed field lines, the precipitation map will look very different.) The area of particle precipitation is complex and large mostly at high northern latitudes, where the particle loss cone is large owing to a less divergent magnetic field there. Figure 24 shows the time distribution of particle precipitation. It is interesting to see that there is a significant long-duration tail. Figure 25 is the latitude-longitude distribution of the magnetic footpoint on the solar wind source surface  $2.5 R_s$  of the escaping particles. Most of the escaping particles are directed toward the northern hemisphere. The longitudinal distribution is broad. At high northern latitudes, the particle intensity is essentially uniform. Figure 26 shows the longitudinal cut of particle distribution in the equator. The distribution deviates from the Gaussian approximation very much even in the core regions of direct particle injection. A tail develops with time at longitudes far away from the directly connected field lines in the core, while particle intensity in the core injection site does not vary much over time. Figure 27 shows the projected particle distribution in the equatorial  $x-y$  plane. The longitudinal spread is remarkable both at high northern latitudes ( $\theta < 60^\circ$ ) and near the equator ( $60^\circ < \theta < 120^\circ$ ).

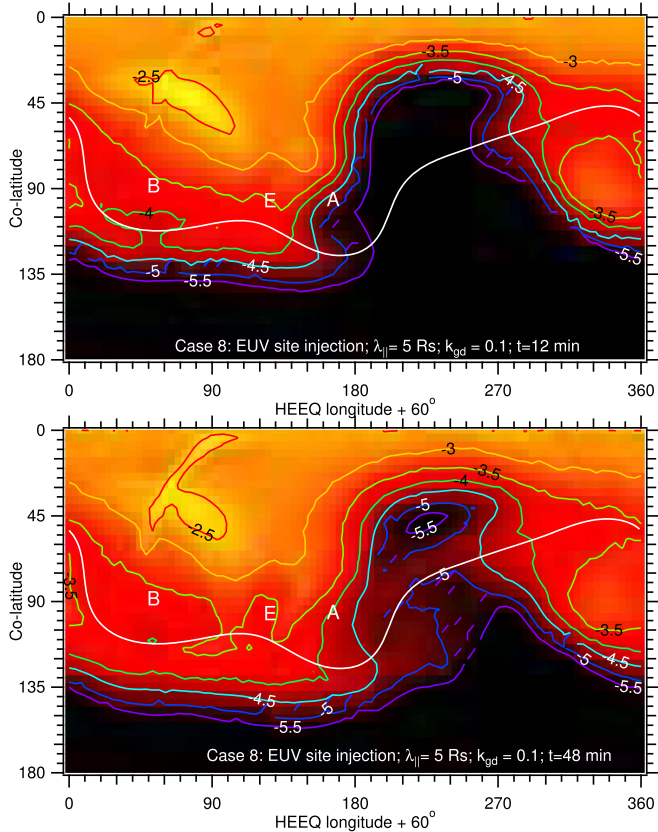


**Figure 25.** Distribution of the magnetic footpoint of escaping particles in the  $\log_{10}$  scale on the solar wind source surface  $2.5 R_s$ .

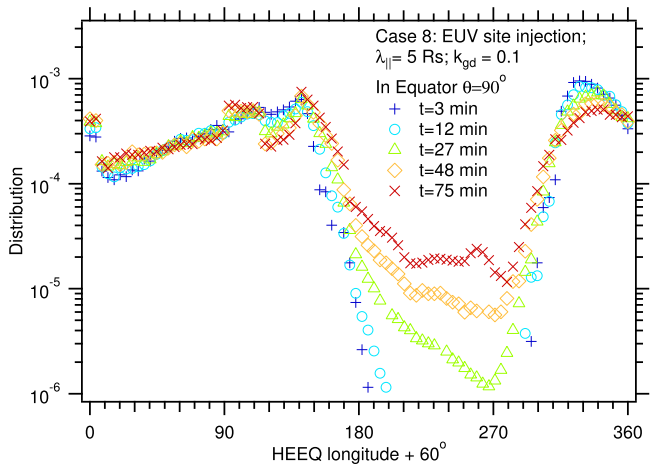


**Figure 26.** Longitudinal distribution of escaping particles in the equatorial plane.

#### 4. Conclusion and Discussion

We have presented the results of our calculation on SEP propagation in the coronal magnetic field using the focus transport equation that includes particle pitch-angle scattering and perpendicular diffusion through meandering field lines. Our model with a PFSS coronal magnetic field is applied to the 2010 February 7 event, in which the two *STEREO* spacecraft and *ACE* saw that SEPs with the characteristics of impulsive

events can spread over a wide range of longitudes. We have derived the following features of SEP propagation for a few scenarios of particle injection, such as at a compact solar flare site, a CME, and an EUV wave of some considerable sizes with different levels of particle scattering and perpendicular diffusion in the corona. Table 1 summarizes the overall behaviors of SEP precipitation and release from the corona under their various conditions of particle injection and transport.

Without perpendicular diffusion, all the models cannot explain the observations of SEPs obtained by *ACE* and *STEREO-A* on magnetic field lines far away from the solar flare or CME, even though the complexity of the coronal magnetic field has been fully considered. If the random walk of magnetic field lines in the photosphere is on order of 10% of the supergranular diffusion rate, the amount of particle perpendicular diffusion by following the meandering of field lines in the corona and interplanetary space is enough to account for the SEP longitudinal spread from the compact solar flare site to a wide longitudinal separation spanned by the two *STEREO* spacecraft and *ACE* in this event. There is little difference as to whether the particles are injected at the compact solar flare site or on a broad CME shock front centered around the solar flare. A more extended EUV wave may further distribute the particles to a wider region. The latitude-longitude distribution of SEPs released into the interplanetary space has its own spatial pattern depending on the detailed magnetic field structure in the corona. While the longitudinal spread of SEPs can be broad, there are certain regions where SEPs still cannot easily access. These features can explain why SEPs are seen over a wide range of longitudes and latitudes, but sometimes one spacecraft or two may completely miss it. If the coronal magnetic field is more disturbed, particles tend to be held back in the corona by enhanced pitch-angle scattering. A slight delay of SEP escape from the corona by a few minutes to tens of minutes can result in an increase of particle spread in longitude and latitude through perpendicular diffusion. Our model predicts that SEPs after multiple CME and solar flare events tend to spread more easily in longitude and latitude. If the random walk of the magnetic field lines in the corona is weak, say, less than 1% of the supergranular diffusion, we find that SEPs from the 2010 February 7 event cannot be explained by particles released from a compact site around the solar flare.

SEPs injected in solar flares or CMEs can also precipitate downward onto the photosphere, where they are absorbed by collisional loss with the ambient gas. The percentage of precipitating particles is typically much less than the escaping particles. Gamma rays (and neutrons from SEP ions) could be produced as nonthermal emissions. The pattern of these emissions can be more complicated than we normally think. Without perpendicular diffusion of particles, particles can only get to the photosphere through direct field line connection. However, even with a small amount of perpendicular diffusion, particles can get to closed or unconnected open field lines. Eventual particle precipitation on these field lines can produce a complicated image pattern of gamma-ray emissions. Gamma rays may come out from regions where no solar flare or CME is seen. This can provide us the opportunity to explore the mechanisms of particle acceleration and transport, as well as magnetic field structure in the corona.

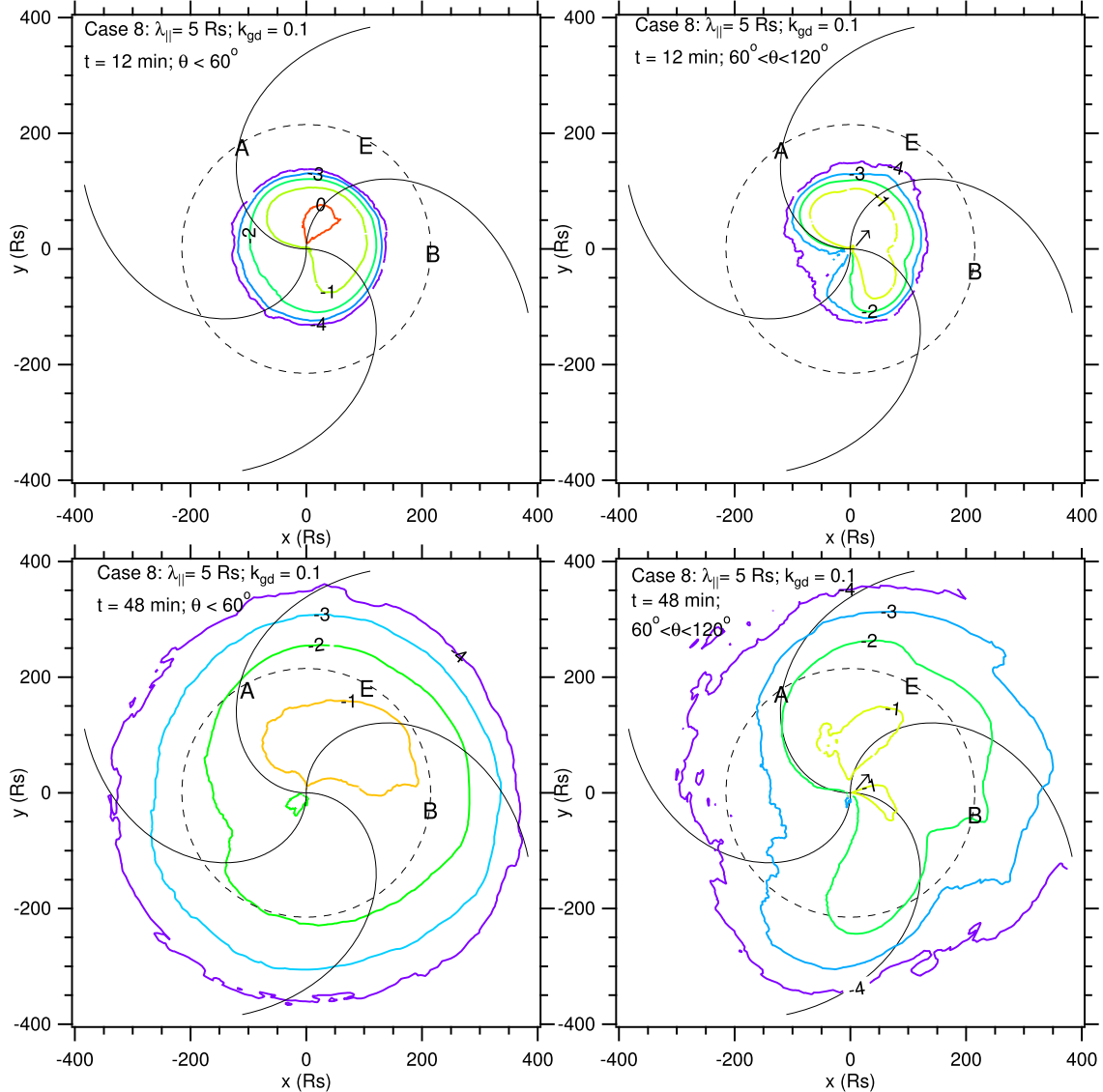


**Figure 27.** Distribution of escaping particles projected along the meridian to the equatorial  $x$ - $y$  plane. The locations of *STEREO-B*, Earth, and *STEREO-A* are labeled by the letters B, E, and A, respectively. The arrow indicates the direction of solar flare longitude.

**Table 1**  
Characteristics of SEP Propagation Simulation Runs

Case	Injection		Transport		Precipitation		Escaping SEP Lateral Expansion
	Site	Height	Parallel	Perpendicular	Site	Intensity	
0A			$\lambda_{  } = 5 R_s$	$k_{gd} = 0$	Single	7.6%	None
0B	Flare site $5^\circ$		$\lambda_{  } = 0.5 R_s$	$k_{gd} = 0$	Single	8.7%	None
1	Open field	$1.05 R_s$	$\lambda_{  } = 5 R_s$	$k_{gd} = 0.1$	Multiple	16%	Adequate
2			$\lambda_{  } = 5 R_s$	$k_{gd} = 0.01$	Multiple	10%	Weak
3			$\lambda_{  } = 0.5 R_s$	$k_{gd} = 0.1$	Multiple	22%	Adequate
0C	Flare site $5^\circ$		$\lambda_{  } = 5 R_s$	$k_{gd} = 0$	Multiple	100%	None
0D	Closed field	$1.05 R_s$	$\lambda_{  } = 0.5 R_s$	$k_{gd} = 0$	Multiple	100%	None
4			$\lambda_{  } = 5 R_s$	$k_{gd} = 0$	Multiple	1.9%	None
5	CME $45^\circ$	$1.5 R_s$	$\lambda_{  } = 5 R_s$	$k_{gd} = 0.1$	Extended	3.9%	Adequate
6	Open field		$\lambda_{  } = 0.5 R_s$	$k_{gd} = 0.1$	Extended	13%	Adequate
7		$2.5 R_s$	$\lambda_{  } = 5 R_s$	$k_{gd} = 0.1$	Extended	1.1%	Adequate
8	EUV wave $75^\circ$	$1.05 R_s$	$\lambda_{  } = 5 R_s$	$k_{gd} = 0.1$	Extended	26%	Adequate

We have the PFSS model for the coronal magnetic field in our calculations. The fidelity of the PFSS model is probably okay for the global structure, but on small scales the model magnetic field could be terrible in predicting the reality. If we want to look at the detailed pattern of particle precipitation, the model may produce very different geometries, particularly those weak precipitation sites. So the above calculation results of particle precipitation can only be taken in a qualitative manner. The escape of SEPs from the corona is a little more certain, subject to the uncertainty levels of particle pitch-angle scattering and perpendicular diffusion. The model can be further improved with a more realistic solar wind model that allows nonradial expansion of the solar wind and embedded magnetic field in the outer corona.

This work was supported in part by NSF grant AGS-1156056 and NASA grants NNX14AJ53G, NNX15AN72G, and NNX15AB76G. We highly appreciate discussions with NASA Living With the Star focus science team members collaborating on studying the physics-based methods to predict connectivity of SEP sources to points in the inner heliosphere, tested by location, timing, and longitudinal separation of SEPs. M.Z. would like to thank Andrew R. Marble of NSO for generating one of the figures used in the paper. We acknowledge using the computation facility funded by NSF MRI grant 0923050 at the Florida Institute of Technology.

## ORCID iDs

Ming Zhang  <https://orcid.org/0000-0003-3529-8743>

## References

- Altschuler, M. D., & Newkirk, G. 1969, *SoPh*, **9**, 131  
 Bieber, J. W., Matthaeus, W. H., Smith, C. W., et al. 1994, *ApJ*, **420**, 294  
 Bučík, R., Innes, D. E., Mason, M., & Wiedenbeck, M. E. 2016, *ApJ*, **833**, 63  
 Chollet, E. E., & Giacalone, J. 2011, *ApJ*, **728**, 64  
 Cliver, E. W., Kahler, S. W., Neidig, D. F., et al. 1995, Proc. ICRC (Rome), **4**, 257  
 Dalla, S., Balogh, A., Krucker, S., et al. 2003, *GeoRL*, **30**, 8035  
 Dresing, N., Gómez-Herrero, R., Heber, B., et al. 2014, *A&A*, **567**, 27  
 Dresing, N., Gómez-Herrero, R., Klassen, A., et al. 2012, *SoPh*, **281**, 281  
 Dröge, W., Kartavykh, Y. Y., Dresing, N., Heber, B., & Klassen, A. 2014, *JGRA*, **119**, 6074  
 Dröge, W., Kartavykh, Y. Y., Dresing, N., & Klassen, A. 2016, *ApJ*, **826**, 134  
 Dröge, W., Kartavykh, Y. Y., Klecker, B., & Kovaltsov, G. A. 2010, *ApJ*, **709**, 912  
 Dwyer, J. R., Mason, G. M., Mazur, J. E., et al. 1997, *ApJ*, **490**, 115  
 Ferreira, S. E. S., Potgieter, M. S., Burger, R. A., et al. 2001, *JGR*, **106**, 29313  
 Giacalone, J., & Jokipii, J. R. 1999, *ApJ*, **520**, 204  
 Gómez-Herrero, R., Dresing, N., Klassen, A., et al. 2015, *ApJ*, **799**, 55  
 Haggerty, D. K., & Roelof, E. C. 2002, *ApJ*, **579**, 841  
 Hasselmann, K., & Wibberenz, G. 1970, *ApJ*, **162**, 1049  
 He, H.-Q., Qin, G., & Zhang, M. 2011, *ApJ*, **734**, 74  
 He, H.-Q., & Wan, W. 2017, *MNRAS*, **464**, 85  
 Isenberg, P. A. 1997, *JGR*, **102**, 4719  
 Jackson, J. D. 1999, Classical Electrodynamics (3rd ed.; New York: Wiley)  
 Jokipii, J. R. 1966, *ApJ*, **146**, 480  
 Klein, K.-L., Krucker, S., Lointier, G., & Kerdraon, A. 2008, *A&A*, **486**, 589  
 Lario, D., Kwon, R.-Y., Richardson, I. G., et al. 2017, *ApJ*, **838**, 51  
 Lario, D., Kwon, R.-Y., Vourlidas, A., et al. 2016, *ApJ*, **819**, 72  
 Lario, D., Raouafi, N. E., Kwon, R.-Y., et al. 2014, *ApJ*, **797**, 8  
 Leblanc, Y., Dulk, G. A., & Bougeret, J. 1998, *SoPh*, **183**, 165  
 Masson, S., Antiochos, S. K., & DeVore, C. R. 2013, *ApJ*, **771**, 82  
 Matthaeus, W. H., Qin, G., Bieber, J. W., & Zank, G. P. 2003, *ApJ*, **590**, 53  
 Mazur, J. E., Mason, G. M., Dwyer, J. R., et al. 2000, *ApJL*, **532**, 79  
 McKibben, R. B. 1972, *JGR*, **77**, 3975  
 McKibben, R. B., Lopate, C., & Zhang, M. 2001, *SSRv*, **97**, 257  
 Meyer-Vernet, N., & Issautier, K. 1998, *JGR*, **103**, 29705  
 Northrop, T. G. 1963, *RvGSP*, **1**, 283  
 Perez, J. C., & Chandran, B. D. G. 2013, *ApJ*, **776**, 124  
 Potgieter, M. S. 2000, *JGR*, **105**, 18295  
 Prise, A. J., Harra, L. K., Matthews, S. A., Long, D. M., & Aylward, A. D. 2014, *SoPh*, **289**, 1731  
 Qin, G., Matthaeus, W. H., & Bieber, J. W. 2002, *ApJ*, **578**, 117  
 Qin, G., & Wang, Y. 2015, *ApJ*, **809**, 177  
 Qin, G., Wang, Y., Zhang, M., & Dalla, S. 2013, *ApJ*, **766**, 74  
 Qin, G., Zhang, M., & Dwyer, J. R. 2006, *JGRA*, **111**, 8101  
 Qin, G., Zhang, M., Dwyer, J. R., & Rassoul, H. K. 2004, *ApJ*, **609**, 1076  
 Qin, G., Zhang, M., Dwyer, J. R., Rassoul, H. K., & Mason, G. M. 2005, *ApJ*, **627**, 562  
 Qin, G., & Zhang, T.-L. 2014, *ApJ*, **787**, 12  
 Reames, D. V. 1999, *SSRv*, **90**, 413  
 Richardson, I. G., Cane, H. V., & von Rosenvinge, T. T. 1991, *JGR*, **96**, 7853  
 Rieutord, M., & Rincon, F. 2010, *LRSP*, **7**, 82  
 Roelof, E. C. 1969, in Lectures on High-Energy Astrophysics, ed. H. Ögelman & J. R. Wayland (NASA SP-199; Washington, DC: NASA), 111  
 Roelof, E. C., Gold, R. E., Simmett, G. M., et al. 1992, *GeoRL*, **19**, 1243  
 Rouillard, A. P., Sheeley, N. R., Tylka, A., et al. 2012, *ApJ*, **752**, 44  
 Ruffolo, D. 1995, *ApJ*, **442**, 861  
 Schlickeiser, R. 2002, Cosmic Ray Astrophysics (Berlin: Springer)  
 Schrijver, C. J., Title, A. M., Yeates, A. R., & DeRosa, M. L. 2013, *ApJ*, **773**, 93  
 Skillings, J. 1971, *ApJ*, **170**, 265  
 Shalchi, A., & Hussein, M. 2014, *ApJ*, **794**, 56  
 Spitzer, L. 1962, Physics of Fully Ionized Gases (New York: Interscience)  
 Wang, Y., Qin, G., & Zhang, M. 2012, *ApJ*, **752**, 37  
 Wang, Y., Qin, G., Zhang, M., & Dalla, S. 2014, *ApJ*, **789**, 157  
 Wiedenbeck, M. E., Mason, G. M., Cohen, C. M. S., et al. 2013, *ApJ*, **1762**, 54  
 Zhang, M. 2006, *JGRA*, **111**, 4208  
 Zhang, M., Jokipii, J. R., & McKibben, R. B. 2003a, *ApJ*, **595**, 493  
 Zhang, M., McKibben, R. B., Lopate, C., et al. 2003b, *JGRA*, **108**, 1154  
 Zhang, M., Qin, G., & Rassoul, H. 2009, *ApJ*, **692**, 109  
 Zhang, M., Qin, G., Rassoul, H., et al. 2007, *P&SS*, **55**, 12  
 Zuo, P., Zhang, M., & Rassoul, H. K. 2013, *ApJ*, **776**, 93